

GSCo: Towards Generalizable AI in Medicine via Generalist-Specialist Collaboration

Sunan He^{1†}, Yuxiang Nie^{1†}, Hongmei Wang¹, Shu Yang¹,
Yihui Wang¹, Zhiyuan Cai¹, Zhixuan Chen¹, Yingxue Xu¹,
Luyang Luo², Huiling Xiang³, Xi Lin³, Mingxiang Wu⁴,
Yifan Peng⁵, George Shih⁶, Ziyang Xu⁷, Xian Wu⁸, Qiong Wang⁹,
Ronald Cheong Kin Chan^{10, 11}, Varut Vardhanabhuti¹²,
Winnie Chiu Wing Chu¹³, Yefeng Zheng¹⁴, Pranav Rajpurkar²,
Kang Zhang¹⁵, Hao Chen^{1,16,17,18,19*}

¹Department of Computer Science and Engineering, The Hong Kong
University of Science and Technology, Hong Kong, China.

²Department of Biomedical Informatics, Harvard University, Boston,
USA.

³Department of Ultrasound, Sun Yat-sen University Cancer Center,
Guangzhou, China.

⁴Department of Radiology, Shenzhen People's Hospital, Shenzhen, China.

⁵Population Health Sciences, Weill Cornell Medicine, New York, USA.

⁶Department of Radiology, Weill Cornell Medicine, New York, USA.

⁷Perelman Department of Dermatology, New York Langone Health, New
York, USA.

⁸Jarvis Research Center, Tencent YouTu Lab, Shenzhen, China.

⁹Shenzhen Institute of Advanced Technology, Chinese Academy of
Sciences, Shenzhen, China.

¹⁰Department of Anatomical and Cellular Pathology, The Chinese
University of Hong Kong, Hong Kong, China.

¹¹State Key Laboratory of Translational Oncology, The Chinese
University of Hong Kong, Hong Kong, China.

¹²Department of Diagnostic Radiology, The University of Hong Kong,
Hong Kong, China.

¹³Department of Imaging and Interventional Radiology, The Chinese
University of Hong Kong, Hong Kong, China.

¹⁴Medical Artificial Intelligence Laboratory, Westlake University,
Hangzhou, China.

¹⁵Faculty of Medicine, The Macau University of Science and Technology,
Macao, China.

¹⁶Department of Chemical and Biological Engineering, The Hong Kong
University of Science and Technology, Hong Kong, China.

¹⁷Division of Life Science, The Hong Kong University of Science and
Technology, Hong Kong, China.

¹⁸State Key Laboratory of Molecular Neuroscience, The Hong Kong
University of Science and Technology, Hong Kong, China.

¹⁹Shenzhen-Hong Kong Collaborative Innovation Research Institute,
The Hong Kong University of Science and Technology, Shenzhen, China.

*Corresponding author(s). E-mail(s): jhc@cse.ust.hk;

†These authors contributed equally to this work.

Abstract

Generalist foundation models (GFMs) are renowned for their exceptional capability and flexibility in effectively generalizing across diverse tasks and modalities. In the field of medicine, while GFMs exhibit superior generalizability based on their extensive intrinsic knowledge as well as proficiency in instruction following and in-context learning, specialist models excel in precision due to their in-depth domain-specific knowledge. In this work, for the first time, we explore the synergy between the GFM and specialist models, to enable precise medical image analysis on a broader scope. Specifically, we propose a novel cooperative framework, **Generalist-Specialist Collaboration (GSCo)**, which consists of two stages, namely the construction of GFM and specialists, and collaborative inference on downstream tasks. In the construction stage, we develop **MedDr**, the largest open-source GFM tailored for medicine, showcasing exceptional instruction-following and in-context learning capabilities. Meanwhile, a series of lightweight specialists are crafted for specific downstream tasks with low computational overhead. In the collaborative inference stage, we introduce two cooperative mechanisms, Mixture-of-Expert Diagnosis (MoED) and Retrieval-Augmented Diagnosis (RAD), to harvest the generalist’s in-context learning abilities alongside the specialists’ domain expertise. Concretely, MoED incorporates predictions from specialists as references, while RAD employs specialists to retrieve similar cases, collectively providing MedDr with much more contextual guidance. For a comprehensive evaluation, we curate a large-scale benchmark featuring 28 datasets and about 250,000 images across a wide range of medical modalities, including radiology, pathology, dermatology, ophthalmology, and gastroenterology. Extensive experimental results demonstrate that MedDr consistently outperforms state-of-the-art GFMs on downstream datasets. Furthermore, GSCo exceeds both GFMs and specialists across all out-of-domain disease diagnosis datasets. These findings indicate a significant paradigm shift in the clinical

application of GFMs, transitioning from separate models for specific tasks to a collaborative approach between GFMs and specialists. This collaboration enables GFMs to perform precise medical image analysis even in out-of-domain scenarios, enhancing their scalability and sustainability, thereby advancing the frontiers of generalizable AI in medicine.

Keywords: Artificial Intelligence, Generalist Foundation Model, Generalist-Specialist Collaboration, Medical Image Analysis.

1 Introduction

Advanced by the rapid development of Large Language Models (LLMs) [Achiam et al \(2023\)](#); [Touvron et al \(2023\)](#); [Anil et al \(2023\)](#) as well as vision-language pre-training [Radford et al \(2021\)](#); [Tung et al \(2024\)](#); [Xu et al \(2024\)](#), large-scale vision-language models (LVLMs) [Zhu et al \(2023\)](#); [Liu et al \(2023\)](#); [Chen et al \(2023\)](#) have demonstrated remarkable performance in a wide range of tasks (e.g., visual question answering [Antol et al \(2015\)](#) and image captioning [Lin et al \(2014\)](#)), thus establishing themselves as generalist foundation models (GFMs). In the realm of medicine, GFMs [Li et al \(2024\)](#); [Moor et al \(2023b\)](#); [Wu et al \(2023b\)](#); [Tu et al \(2024\)](#); [Moor et al \(2023a\)](#); [Zhou et al \(2024\)](#); [Saab et al \(2024\)](#); [Yang et al \(2024\)](#) also showcased impressive proficiency in generalizing across various tasks, such as visual question answering [He et al \(2020\)](#); [Ben Abacha et al \(2019\)](#) and radiology report generation tasks [Johnson et al \(2019\)](#); [Demner-Fushman et al \(2016\)](#); [Jin et al \(2024\)](#); [Chen et al \(2024b\)](#). The remarkable generalizability of GFMs can be attributed to two key aspects. First, the extensive and diverse training corpus endows the models with comprehensive medical knowledge. Additionally, the powerful instruction following and in-context learning abilities of GFMs improve their versatility and flexibility, facilitating their applications across a multitude of tasks. While GFMs exhibit superior generalizability, specialist models excel in precision. Tailored for specific downstream tasks, these specialist models possess profound domain-specific knowledge, enabling themselves to concentrate on a narrower scope and deliver more precise results. For instance, in medical image diagnosis tasks [Nguyen et al \(2021\)](#); [Yang et al \(2023\)](#); [Wang et al \(2023\)](#), specialist models surpass the GFMs and demonstrate superior performance [Tu et al \(2024\)](#); [Hu et al \(2024\)](#); [Chen et al \(2024a\)](#). Therefore, exploring how to utilize the generalizability and flexibility of the GFMs, along with the expertise and precision of specialist models, represents a promising direction for generalizable AI in medicine.

In this work, for the first time, we propose a novel cooperative framework, **Generalist-Specialist Collaboration (GSCo)**, to explore the synergy between the GFMs and specialist models. **Fig. 1 (a)** presents the overview of the GSCo framework, which consists of two stages: the construction of GFM and specialists, and collaborative inference on downstream tasks. In the construction stage, a medical GFM, **MedDr**, is developed based on a large-scale training corpus of medical image-text pairs across various modalities. Meanwhile, a series of lightweight specialist models are

tailored to specific downstream tasks with much lower computational consumption. In the collaborative inference stage, two core mechanisms, namely **Mixture-of-Expert Diagnosis (MoED)** and **Retrieval-Augmented Diagnosis (RAD)**, are proposed to achieve cooperation between MedDr and the specialist models.

Specifically, in the construction stage, we focus on the development of an advanced medical GFM. To curate a large-scale multi-modal training corpus, we introduce two novel datasets: the Diagnosis-Guided Bootstrapping (DGB) dataset and the Medical Image Description (DES) dataset. The DGB dataset is constructed based on abundant medical image diagnosis data [Pham et al \(2022\)](#); [Tschandl et al \(2018\)](#); [Panchal et al \(2023\)](#); [Wang et al \(2017\)](#); [Pacheco et al \(2020\)](#); [Smedsrud et al \(2021\)](#), aiming to enhance the intrinsic disease diagnosis capabilities of the GFM. In contrast to prior methods [Li et al \(2024\)](#); [Wu et al \(2023b\)](#) that solely rely on textual information of image-text pairs to generate instruction-tuning data, the DGB dataset is generated by integrating both visual and textual information. Concretely, we utilize the GFM [Chen et al \(2023\)](#) in the general domain to generate detailed medical reports, including findings and conclusions, based on diagnosis information (e.g., classification labels). Guided by these human-verified annotations, the generated data not only demonstrates increased reliability but also significantly enriches the depth and diversity of visual information conveyed in the text. Additionally, the DES dataset is presented to broaden the scope of the training data, incorporating image-based case studies corresponding to diverse medical conditions from OpenI [Demner-Fushman et al \(2012\)](#). We also employ a GFM [Chen et al \(2023\)](#) to rewrite the text of the case study and remove the information that cannot be derived from the corresponding image. In addition to DGB and DES datasets, we incorporate existing Medical Image Diagnosis (CLS) [Tschandl et al \(2018\)](#), Medical Report Generation (MRG) [Johnson et al \(2019\)](#), and Visual Question Answering (VQA) [Lau et al \(2018\)](#) datasets as well. Overall, the training corpus consists of more than 2 million samples across five distinct types of training datasets, covering a wide range of medical modalities. **Fig. 1 (b)** presents the distribution of the training corpus and two samples from the DGB and DES datasets respectively.

Building upon the training corpus, we develop **MedDr**, the largest open-source generalist foundation model for medicine consisting of 40B parameters. Compared to other generalist foundation models for medicine [Li et al \(2024\)](#); [Moor et al \(2023b\)](#); [Wu et al \(2023b\)](#), MedDr exhibits superior capabilities in medical image analysis across more diverse medical modalities, including radiology, pathology, dermatology, ophthalmology, and gastroenterology. Moreover, MedDr demonstrates advanced in-context learning and instruction-following capability, fostering the collaboration between the generalist foundation model and the specialist models.

In the collaborative inference stage of the GSCo framework, we delve into the synergistic relationship between MedDr and specialist models. To exploit the generalist’s in-context learning abilities alongside the specialists’ domain expertise, mixture-of-expert diagnosis (MoED), and retrieval-augmented diagnosis (RAD) are proposed as the core mechanisms of the collaboration between GFMs and specialists. Mixture-of-expert diagnosis aims to boost the generalist foundation model with the prediction

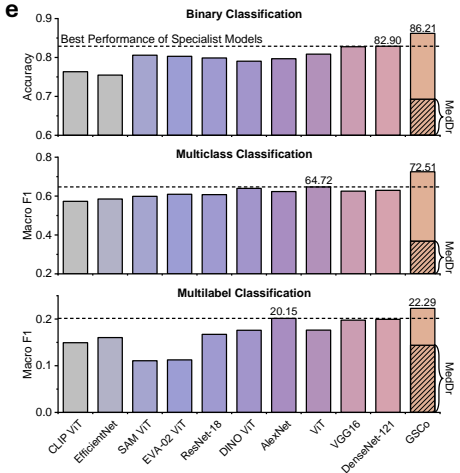
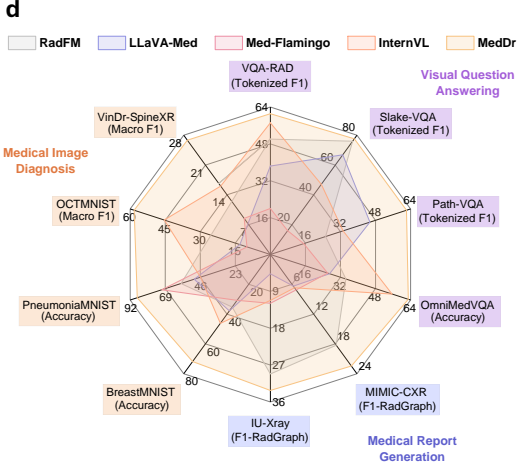
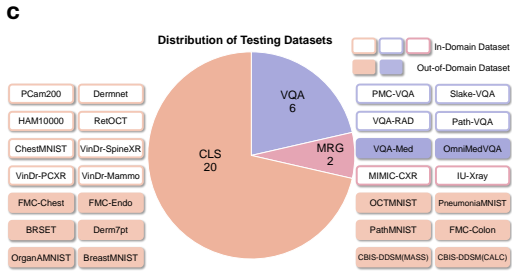
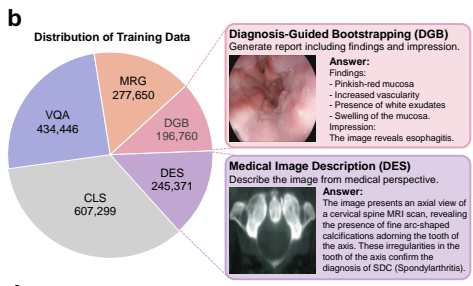
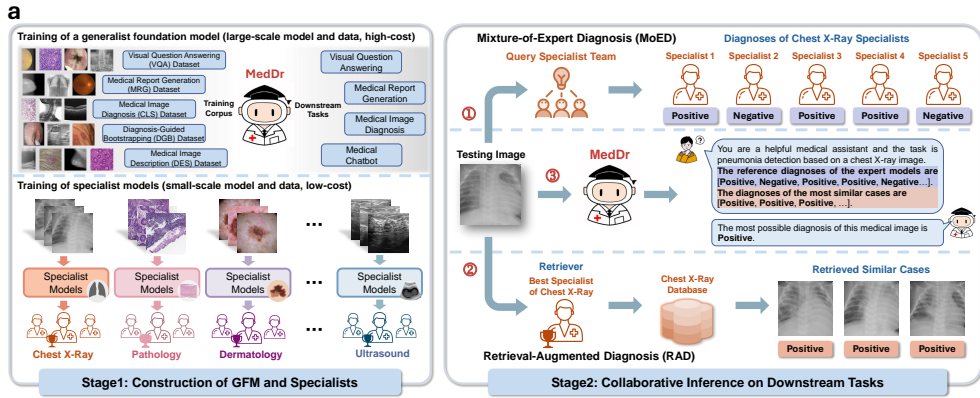


Fig. 1: Overview of the study. (a) Generalist-Specialist Collaboration (GSCo) Framework. In the construction stage, based on a large-scale training corpus, MedDr is developed, capable of performing diverse tasks and handling various medical modalities, demonstrating exceptional generalizability. Meanwhile, a series of specialist models are tailored for distinct tasks on specific datasets with low computational cost, excelling in expertise and precision. In the collaborative inference stage, mixture-of-expert diagnosis (MoED) and retrieval-augmented diagnosis (RAD) are introduced to facilitate collaboration between MedDr and specialist models. MoED incorporates the diagnoses of specialist models as guidance, while RAD utilizes the specialist models to retrieve the most similar cases for reference. The results of MoED and RAD are combined together as the context information fed into the MedDr. (b) Distribution of the training datasets. Two examples of the proposed Diagnosis-Guided Bootstrapping (DGB) and Medical Image Description (DES) data are presented. (c) Distribution of the testing datasets. The benchmark incorporates 14 in-domain datasets and 14 out-of-domain datasets. (d) Performance of the GFMs. MedDr surpasses other GFMs, achieving state-of-the-art performance on diverse medical tasks across various medical modalities. (e) Overall Performance on medical image diagnosis tasks. GSCo excels through the synergy between MedDr and specialist models.

results of specialist models (**Fig. 1 (a)** and **Fig. 8**). The paradigm of mixture-of-expert [Jacobs et al \(1991\)](#), which ensembles the insights from multiple experts, has been explored to enhance the robustness of the predictions [Fedus et al \(2022\)](#); [Luo et al \(2024\)](#); [Xiong et al \(2024\)](#). In MoED, the outputs of the specialist models act as the reference context and are fed into MedDr with the testing image together. Then, MedDr is required to provide the diagnosis considering both the content of the testing image and the results provided by the specialist models. Different from MoED, which exploits the inherent expert knowledge of the specialist model, retrieval-augmented diagnosis is proposed to fully leverage the broad medical knowledge embedded within the existing data (**Fig. 1 (a)** and **Fig. 9**). In contrast to previous medical generalist foundation models [Li et al \(2024\)](#); [Moor et al \(2023b\)](#); [Wu et al \(2023b\)](#); [Tu et al \(2024\)](#) that relied solely on the internal knowledge of the model to make diagnoses, we incorporate Retrieval-Augmented Generation (RAG) [Lewis et al \(2020\)](#) to leverage external knowledge, thereby enhancing model accuracy and reliability. Concretely, in the proposed RAD mechanism, each specialist model serves as a retriever, using the visual embedding of the testing image as the query to retrieve the most similar samples in the database. The information from the retrieved samples is then provided to the generalist foundation model as a contextual reference to assist medical image analysis. MoED and RAD collectively provide helpful guidance to MedDr based on the expertise of the specialists. Meanwhile, as a decision-maker, MedDr integrates its intrinsic knowledge with external knowledge to render the final diagnosis.

To comprehensively evaluate MedDr and the proposed GSCo framework, we curate a large-scale benchmark. Compared with previous works [Li et al \(2024\)](#); [Moor et al \(2023b\)](#); [Wu et al \(2023b\)](#); [Tu et al \(2024\)](#); [Zhang et al \(2024\)](#), this benchmark excels in both diversity and magnitude. As shown in **Fig. 1 (c)**, it encompasses diverse

medical datasets such as medical image diagnosis, visual question answering, medical report generation tasks, etc. Specifically, there are 14 in-domain datasets and 14 out-of-domain datasets, resulting in a total of 250,000 samples. Notably, to assess the improvements brought by GSCo to GFM on medical image diagnosis datasets, where specialists often yield superior results due to their domain-specific knowledge, we integrate 20 distinct medical image diagnosis datasets, including 11 medical modalities.

We first conduct experiments on GFMs to demonstrate the superiority of MedDr. **Fig. 1 (d)** presents the comparison among GFMs on 10 benchmark datasets that span different medical tasks and modalities. MedDr consistently surpasses other GFMs from both medical and general domains by a large margin. We then perform experiments to validate the effectiveness of GSCo. **Fig. 1 (e)** illustrates performance on medical image diagnosis tasks. Despite the competitive performance of specialist models due to their domain-specific knowledge, the proposed GSCo framework further improves the performance of MedDr and surpasses all specialist models. These experimental results highlight the significance of the proposed GSCo framework, representing a paradigm shift in the clinical application of GFMs. This transition moves from utilizing separate models for medical tasks independently to fostering collaboration between GFMs and specialist models. The advantages of the GSCo framework are twofold: Firstly, GSCo is effective. Compared with the independent use of either GFMs or specialist models, GSCo demonstrates superior performance, particularly on out-of-domain datasets, showcasing its advanced generalizability. Secondly, GSCo is efficient. When confronted with out-of-domain tasks or data, rather than investing substantial resources to fine-tune the GFM, it can efficiently adapt lightweight specialist models with minimal consumption, indicating its scalability and sustainability.

To summarize, our contributions are as follows:

- We introduce Generalist-Specialist Collaboration (GSCo), the first collaborative framework to explore the synergy between the GFM and specialist models. GSCo harvests the generalist’s in-context learning ability and the specialists’ domain expertise, to enable precise medical image analysis on diverse medical tasks. This synergistic paradigm not only broadens the functionalities of the GFM with efficient resource utilization but also ensures scalability and sustainability, thereby catalyzing the advancement of generalizable AI in the medical field.
- We present MedDr, the largest open-source generalist foundation model tailored for medicine. Concretely, in the development of MedDr, diagnosis-guided bootstrapping (DGB) and medical image description (DES) are introduced to enhance the diversity of the training corpus. As a result, MedDr can handle various medical modalities and tasks, achieving state-of-the-art performance in downstream tasks and outperforming other GFMs. Additionally, MedDr excels in instruction-following and in-context learning, providing a better foundation for collaboration with specialist models.
- We propose two cooperative mechanisms, mixture-of-expert diagnosis (MoED) and retrieval-augmented diagnosis (RAD), to facilitate collaboration between MedDr and specialist models. MoED incorporates the diagnoses of specialists as guidance, while RAD utilizes the specialists to retrieve the most similar cases for reference. The results of MoED and RAD are combined together as the context information fed into the MedDr as guidance.

- We establish a large-scale benchmark, which comprises 28 datasets with about 250,000 test images, covering more than ten medical modalities across various medical tasks. Extensive experiments are conducted on the benchmark, demonstrating the superior capabilities of MedDr and validating the efficacy of the proposed GSCo framework.

2 Results

Comprehensive evaluation benchmark in medicine

In this study, to thoroughly assess the model’s performance of the medical tasks, we curated a large-scale benchmark, encompassing 28 public datasets comprising about 250,000 images. Compared with previous work [Li et al \(2024\)](#); [Moor et al \(2023b\)](#); [Wu et al \(2023b\)](#); [Tu et al \(2024\)](#); [Zhang et al \(2024\)](#), this benchmark excels in both diversity and magnitude. The datasets within our benchmark are carefully selected to include clinically pertinent tasks such as medical image diagnosis, visual question answering, and medical report generation. Additionally, the benchmark spans a diverse range of medical image modalities, including radiology, pathology, dermatology, ophthalmology, gastroenterology, etc., ensuring a comprehensive evaluation of the model’s capabilities across various medical conditions.

Medical Image Diagnosis

Medical Image Diagnosis is one of the most fundamental tasks in medicine, which requires the model to diagnose the queried images within a predefined label set. In our benchmark, we integrate 20 distinct medical image diagnosis datasets, encompassing approximately 100,000 testing samples and 11 medical modalities. This benchmark has two prominent features. Firstly, the benchmark covers diverse medical conditions. For instance, VinDr-SpineXR [Nguyen et al \(2021\)](#) and FMC-Chest [Wang et al \(2023\)](#) are challenging radiology datasets that focus on spine and chest X-ray images, respectively. HAM10000 [Tschandl et al \(2018\)](#) and DermNet [Goel \(2020\)](#) are both datasets related to skin diseases, with the former focusing more on dermatoscopic images and the latter more on clinical images. RetOCT [Subramanian et al \(2022\)](#) and BRSET [Nakayama et al \(2023\)](#) focus on ocular diseases despite with different medical modalities. Secondly, the benchmark incorporates different classification types. For example, PneumoniaMNIST [Yang et al \(2023\)](#) and BreastMNIST [Yang et al \(2023\)](#) are binary classification datasets. While providing an available answer (i.e., Positive or Negative) for a binary classification task is straightforward for a GFM, achieving accurate predictions is indeed challenging. FMC-Endo [Wang et al \(2023\)](#) and OCTMNIST [Yang et al \(2023\)](#) are multi-class classification datasets with label sets consisting of 5 and 4 labels, respectively. For each given image, the model is required to predict only one label among the predefined label sets. The most challenging task is multi-label classification, where each test image may possess multiple, or even no, labels. For example, ChestMNIST [Wang et al \(2017\)](#) is a multi-label classification dataset consisting of 15 categories, with each sample potentially having one or more positive labels. Such tasks impose greater demands on the model’s disease diagnosis and task

understanding capabilities than binary and multi-class classification tasks. To facilitate comparative analysis, we categorize these medical image diagnosis datasets into two groups: in-domain datasets and out-of-domain datasets, based on whether the training split of the dataset is included in the training corpus of MedDr. Extended Data Table A10 and Extended Data Table A11 illustrate more detailed information about these datasets. For evaluation metrics, we employ accuracy and macro-F1 for these medical image diagnosis tasks. For binary classification datasets, the results are presented in terms of accuracy. For multi-class and multi-label classification datasets, due to the unbalanced distribution of samples across different classes, the results are reported in terms of the Macro-F1 score. Further details regarding the metric employed can be found in Section 4.

Visual Question Answering

Visual Question Answering (VQA) task requires the model to answer the question based on the given image, requiring a thorough comprehension of both the visual and textual information. We conduct experiments on 6 distinct VQA datasets, comprising 4 in-domain datasets: VQA-RAD [Lau et al \(2018\)](#), Slake-VQA [Liu et al \(2021\)](#), Path-VQA [He et al \(2020\)](#), and PMC-VQA [Zhang et al \(2023a\)](#), as well as 2 out-of-domain datasets: VQA-Med [Ben Abacha et al \(2019\)](#) and OmniMedVQA [Hu et al \(2024\)](#). The diversity inherent in these benchmark datasets allows us to extract valuable insights across various domains and facilitates a thorough evaluation of model performance. For example, VQA-RAD, Slake-VQA, and VQA-Med datasets primarily focus on radiology data, such as CT, MRI, and X-ray images, while Path-VQA is mainly about pathology data. In contrast, the PMC-VQA and OmniMedVQA datasets are larger in scale and cover a broader spectrum of medical modalities. PMC-VQA is built on PubMed while OmniMedVQA is derived from a wide range of medical datasets. Notably, aside from OmniMedVQA, which consists of multiple-choice questions, the other datasets contain free-form questions. For the evaluation of OmniMedVQA, we employ accuracy as our metric. For other datasets, following MultiMedEval [Royer et al \(2024\)](#), we evaluate the results using both natural language generation (NLG) and classification metrics.

Medical Report Generation

Medical Report Generation (MRG) involves the model’s ability to enumerate all observations and deliver a diagnosis based on the analysis of the medical image. This task presents a significant challenge, as it requires the model to accurately capture the complexities inherent in the medical images being evaluated. To assess the performance of MRG, we conduct experiments on two benchmark datasets, i.e., MIMIC-CXR [Johnson et al \(2019\)](#) and IU-Xray [Demner-Fushman et al \(2016\)](#). Both datasets focus on chest X-ray images and offer detailed medical reports that summarize patient conditions. For the evaluation of the models, we utilize both NLG metrics and model-based metrics in MultiMedEval [Royer et al \(2024\)](#). Further details regarding the metric employed in VQA and MRG tasks can be found in Section 4.

MedDr demonstrates superior performance in medical image diagnosis

We first explore the performance of the GFMs on medical image diagnosis tasks. It should be noted that some GFMs are unable to produce appropriate responses used for evaluation on specific datasets, so we do not include them in the comparison. If the performance of MedDr is the best one compared to other GFMs, the P-value would be presented. The experimental results are illustrated in **Fig.2**. Specifically, **Figs.2(a)-(h)** represent the in-domain results, while **Figs.2(i)-(t)** depict the out-of-domain results. For binary classification datasets (e.g., PCam200), the results are reported in terms of accuracy. For multi-class (e.g., DermNet) and multi-label datasets (e.g., ChestMNIST), the results are presented in terms of macro-F1 score.

Overall, MedDr outperforms other GFMs significantly and demonstrates its superiority in three aspects. Firstly, MedDr is proficient in instruction following. We note that RadFM, LLaVA-Med, and Med-Flamingo occasionally struggle to generate appropriate outputs for tasks that involve multiple labels. For instance, in multi-class classification tasks where only one label exists, they may either output the entire label set or merely rephrase the instructions, suggesting their inferior instruction following capabilities. In contrast, MedDr effectively adheres to instructions across a diverse range of tasks, consistently generating coherent and contextually appropriate outputs. Secondly, MedDr can handle a broader scope of medical modalities. RadFM [Wu et al \(2023b\)](#) is a GFM focusing on the radiology data so that it achieves commendable performance on radiology datasets such as VinDr-SpineXR [Nguyen et al \(2021\)](#) and VinDr-PCXR [Pham et al \(2022\)](#). However, its performance diminishes when applied to other medical modalities, indicating its limited generalization capabilities. In comparison, MedDr is capable of processing diverse medical modalities, including radiology, pathology, dermatology, ophthalmology, gastroenterology, etc. Thirdly, MedDr excels in medical image diagnosis. LLaVA-Med [Li et al \(2024\)](#) and Med-Flamingo [Moor et al \(2023b\)](#) are mainly trained on visual question answering datasets. Their overall performance in medical image diagnosis tasks is still far from satisfactory. Meanwhile, InternVL [Chen et al \(2023\)](#) can follow the instructions well, but its performance still lags MedDr by a large margin due to its limited inherent medical knowledge. For instance, on the FMC-Endo [Wang et al \(2023\)](#) dataset, MedDr obtains a 32.0% Macro-F1 score and significantly outperforms InternVL (11.7% Macro-F1 score, $P < 0.001$, **Fig. 2(r)**). Notably, in some binary classification datasets, such as CBIS-DDSM (CALC) [Sawyer-Lee et al \(2016\)](#) and CBIS-DDSM (MASS) [Sawyer-Lee et al \(2016\)](#), LLaVA-Med, Med-Flamingo and InternVL struggle to distinguish between the two classes, consistently assigning the same label to all samples. Although these models may achieve higher accuracy, their F1 score is 0. This lack of differentiation indicates that these models may fail to capture the pertinent features necessary for effective classification, thereby undermining the reliability of their results. In contrast, MedDr achieves outstanding performance across various medical modalities and classification tasks, thereby highlighting its advanced capabilities in medical image analysis.

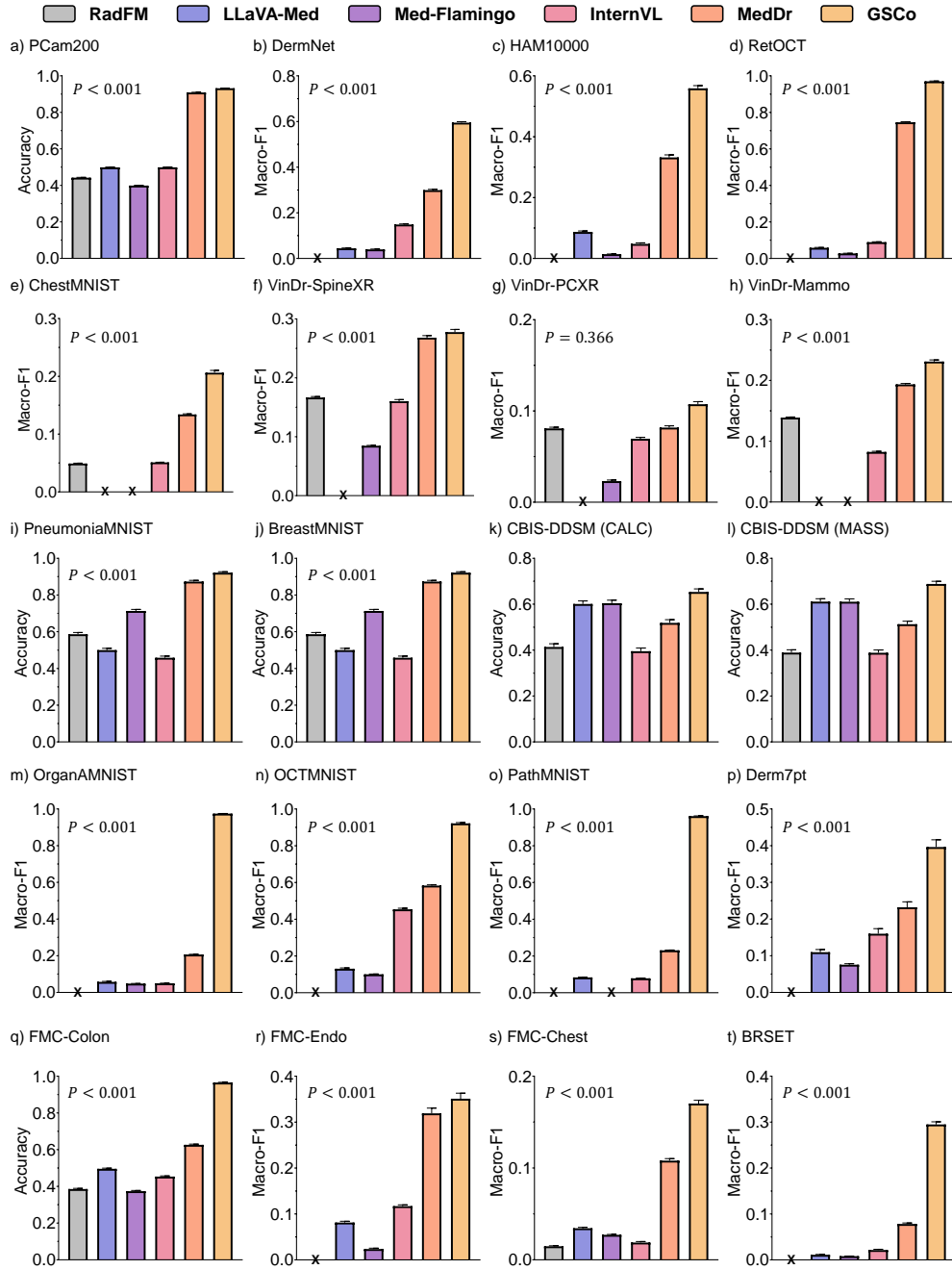


Fig. 2: Experimental results of different GFMs and the GSCo framework on medical image diagnosis datasets. (a)-(h): In-domain datasets. (i)-(t): Out-of-domain datasets. For binary classification datasets (e.g., PCam200), the results are reported in terms of Accuracy. For multi-class (e.g., DermNet) and multi-label datasets (e.g., ChestMNIST), the results are presented in terms of the Macro-F1 score. If the performance of MedDr is the best one compared to other GFMs, P-value would be presented. The model marked with “X” cannot generate an appropriate response to evaluate its performance. Detailed results are presented in **Extended Data Tables A1, A2 and A3**.

MedDr excels in visual question answering and medical report generation

Here, we delve into the evaluation of GFMs in visual question answering and medical report generation tasks. The results of VQA tasks are presented in **Fig. 3(a)-(b)**, **Extended Data Table A4** and **Extended Data Table A5**.

Overall, MedDr consistently outperforms other GFMs across all datasets. Concretely, on the VQA-RAD dataset, MedDr achieves a 59.62% BLEU-1 score ($P = 0.062$) and a 61.10% F1 score ($P = 0.054$), much better than the fine-tuned LLaVA-Med. On the Slake-VQA dataset, MedDr obtains an 83.38% accuracy on close-ended questions and a 77.26% recall, surpassing RadFM by a large margin ($P < 0.001$, **Fig. 3(a)**). For the most challenging dataset PMC-VQA, MedDr achieves a 27.30% recall and a 14.94% accuracy on open questions, outperforming other models significantly ($P < 0.001$, **Extended Data Table A4**). On the OmniMedVQA datasets, as illustrated in **Fig. 3(b)** and **Extended Data Table A6**, MedDr also establishes superior performance across all medical modalities, resulting in 63.0% overall accuracy. The overall performance of MedDr in the visual question answering task demonstrates that the model not only excels in comprehending both visual and textual information but also handles a greater diversity of medical modalities.

The results of MRG tasks are presented in **Fig. 3(c)** and **Extended Data Table A8**. It should be noted that aside from RadFM [Wu et al \(2023b\)](#) and MedDr, other models such as LLaVA-Med [Li et al \(2024\)](#), Med-Flamingo [Moor et al \(2023b\)](#), and InternVL [Chen et al \(2023\)](#) have not been trained on datasets of MRG tasks. MedDr outperforms RadFM [Wu et al \(2023b\)](#) (overall, $P < 0.001$), which mainly focuses on radiology tasks, across nearly all evaluated metrics on both benchmark datasets. For example, MedDr achieves a ROUGE-L score of 22.59 on the MIMIC-CXR dataset and 28.35 on the IU-Xray dataset, highlighting its proficiency in comprehensively interpreting medical images.

Fig. 3(d) presents a challenging case of medical report generation on a chest X-ray image, characterized by the presence of multiple abnormalities in the patient. We compare MedDr with RadFM [Wu et al \(2023b\)](#), which is a GFM specialized in radiology. The outputs from both MedDr and RadFM are evaluated by a qualified radiologist. Notably, MedDr demonstrates superior performance by accurately identifying most abnormalities, including “mild pulmonary edema”, “small bilateral pleural

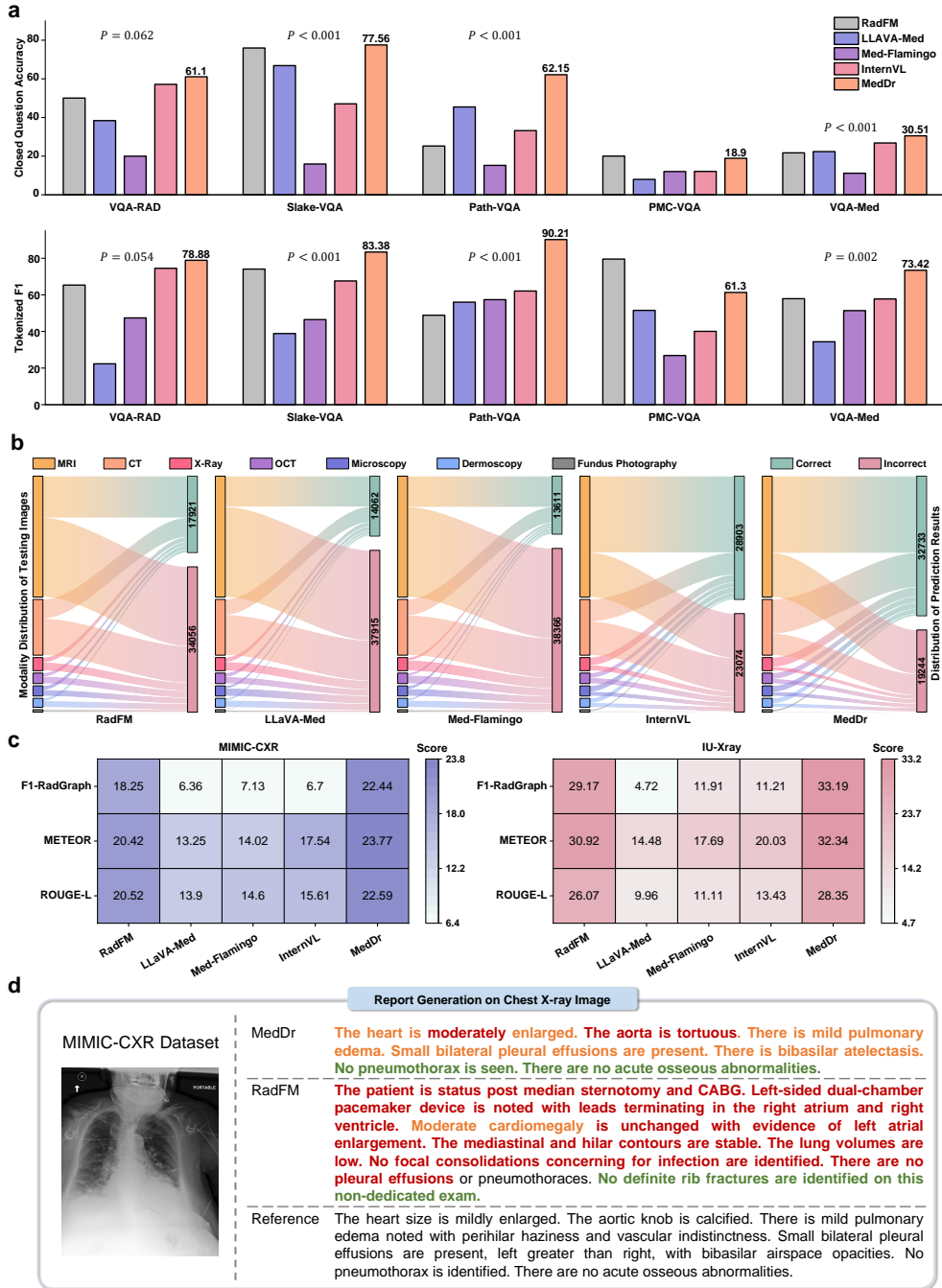


Fig. 3: Experimental results of GFMs on medical visual question answering and medical report generation tasks. (a) Results in terms of Closed Question Accuracy and Tokenized F1-Score on VQA-RAD, Slake-VQA, Path-VQA, PMC-VQA, and VQA-Med datasets. If the performance of MedDr is the best one compared to other GFMs, P-value would be presented. (b) Medical modality and result distribution of the generalist foundation models on the OmnimedVQA dataset. The number refers to the quantity of multiple-choice questions. (c) Results in terms of ROUGE-L, METEOR, F1-RadGraph on medical report generation datasets MIMIC-CXR and IU-Xray. (d) An example of medical report generation on chest X-ray images. The text in **Green** indicates the correct normal contents. The text in **Orange** indicates the correct abnormal contents. The text in **Red** indicates the incorrect contents. Reference denotes the ground truth of the image from the corresponding dataset. Results are accessed by a qualified radiologist. Detailed results are presented in **Extended Data Tables A4, A5, A6, and A8**.

effusions”, and “bibasilar atelectasis”, thereby underscoring its advanced capabilities in the domain of medical image analysis.

GSCo enables accurate disease diagnosis and generalizable AI for medicine

In this section, we conduct experiments on medical image diagnosis datasets to demonstrate the effectiveness of the proposed Generalist-Specialist Collaboration mechanism. Following previous method [Doerrich et al \(2024\)](#), we select ten representative models in computer vision (e.g., ResNet [He et al \(2016\)](#) and ViT [Dosovitskiy et al \(2021\)](#)) as the foundation models, which possess significantly fewer parameters compared to the GFM. Details regarding the selected models can be found in Section 4. We fine-tune these foundation models on each of the 20 medical image diagnosis datasets, resulting in a total of 200 specialist models. Moreover, for a fair comparison, we introduce a baseline method, “Voting”, where results are aggregated and voted from the predictions of the specialists, effectively functioning as a naive collaborative method to exploit the results of the specialist models.

Quantitative Analysis

Fig. 4(a) and **Fig. 4(b)** illustrate the ranking order of various methods on the in-domain datasets and out-of-domain datasets, respectively. The summations of their rankings across different tasks are also presented. Firstly, we observe that MedDr outperforms other GFMs and even surpasses some specialist models on in-domain datasets. Compared with specialist models, the overall performance of GFMs is lower, with most GFMs ranking relatively poorly. This observation indicates that while GFMs demonstrate superior generalizability through performing diverse tasks with a unified model, specialist models excel in precision on specific datasets due to their domain-specific fine-tuning. Notably, on in-domain datasets, MedDr showcases superior performance compared to several specialist models. For instance, on

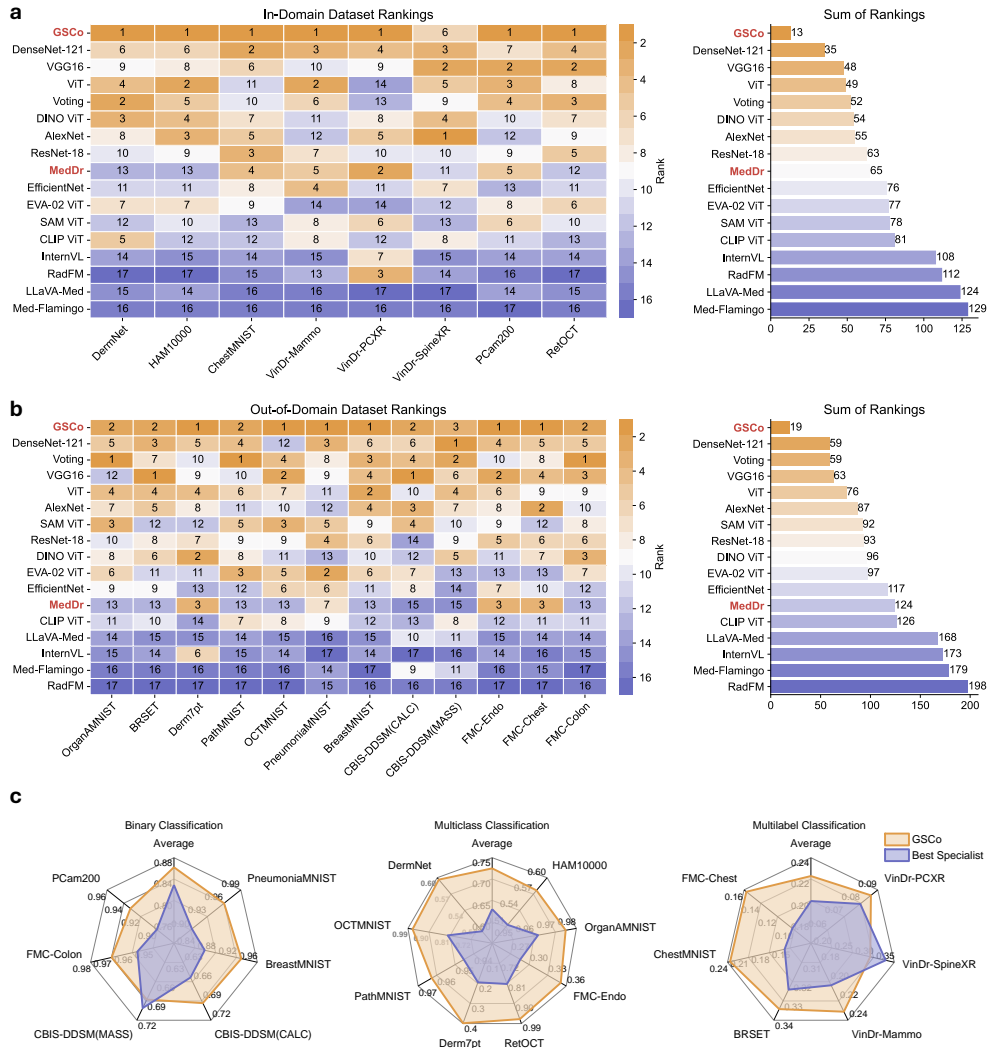


Fig. 4: Overall experimental results on medical image diagnosis datasets. (a) Overall ranking of different models on 8 in-domain datasets and the summation of the rankings. The model with better performance is assigned a lower ranking number. **(b)** Overall ranking of different models on 12 out-of-domain datasets and the summation of the rankings. **(c)** Comparison between the best specialist model DenseNet-121 and the proposed framework GSCo. The datasets are divided into three groups according to the classification types. For binary classification, accuracy is reported. Otherwise, the Macro-F1 score is reported. The detailed experimental results are presented in [Extended Data Tables A1, A2 and A3](#).

the ChestMNIST and PCam200 datasets, MedDr surpasses the majority of specialized models, achieving 4th and 5th place, respectively, which highlights its exceptional intrinsic diagnostic capabilities. Secondly, we find that GSCo achieves the highest overall performance, significantly surpassing other methods. As a straightforward collaborative method, “Voting” shows improvements on most datasets when compared with specialist models, highlighting its effectiveness. However, “Voting” obtains superior performance on binary classification and multi-class classification datasets while acquiring inferior results on multi-label datasets. This discrepancy suggests that it may struggle to effectively leverage the prediction results of specialist models on multi-label classification tasks. This is because, as a naive method, “Voting” relies solely on the outputs of the specialist models and treats their suggestions equally. Consequently, when confronted with highly challenging multi-label classification tasks, if the majority of specialized models provide incorrect predictions, “Voting” may yield erroneous diagnoses. In contrast, the proposed GSCo framework not only considers the predictions from the specialist models but also leverages the inherent knowledge of MedDr, leading to superior performance and robustness. **Fig. 4(c)** presents the comparison between the specialist model with the best overall performance, DenseNet-121, and the proposed framework GSCo. For clarity, the results are categorized into three groups based on their classification task types. Compared with the best specialist model, GSCo exhibits a notable performance advantage, even on out-of-domain datasets, underscoring its superiority and generalizability.

In conclusion, the Generalist-Specialist Collaboration framework exemplifies a synergistic relationship between GFM and specialist models. On the one hand, specialist models, with their domain-specific knowledge, offer guidance to GFM, thereby significantly enhancing its performance, especially on out-of-domain datasets. Additionally, fine-tuning the specialist model on specific downstream datasets is computationally efficient and can be implemented with minimal additional resources. On the other hand, the GFM acts as decision-makers with extensive intrinsic medical knowledge. Different from the “Voting” method, which relies solely on the outputs of specialist models, MedDr retains its diagnostic capabilities while integrating the guidance from these specialists. This collaborative strategy effectively bolsters performance across a wide range of medical tasks.

Qualitative Analysis

We visualize the experimental results of mixture-of-expert diagnosis (MoED) and retrieval-augmented diagnosis (RAD). **Fig. 5(a)-(c)** and **Extended Data Fig. A2** showcase examples of the MoED on downstream datasets across various medical modalities. Firstly, we find that the aggregation of predictions from multiple specialist models yields accurate and robust guidance. In medical image diagnosis, the key to accurately identifying a disease often lies in the subtle nuances present within the image. Due to this inherent difficulty, among all specialist models, only EfficientNet-B4 [Tan and Le \(2019\)](#) consistently produces correct diagnostic results across all example cases. Meanwhile, the aggregation of predictions from multiple specialist models, such as “Voting”, can derive more accurate results. For instance, on the RetOCT dataset (**Fig. 5 (a)**) and CBIS-DDSM(CALC) dataset (**Fig. 5 (b)**), the majority

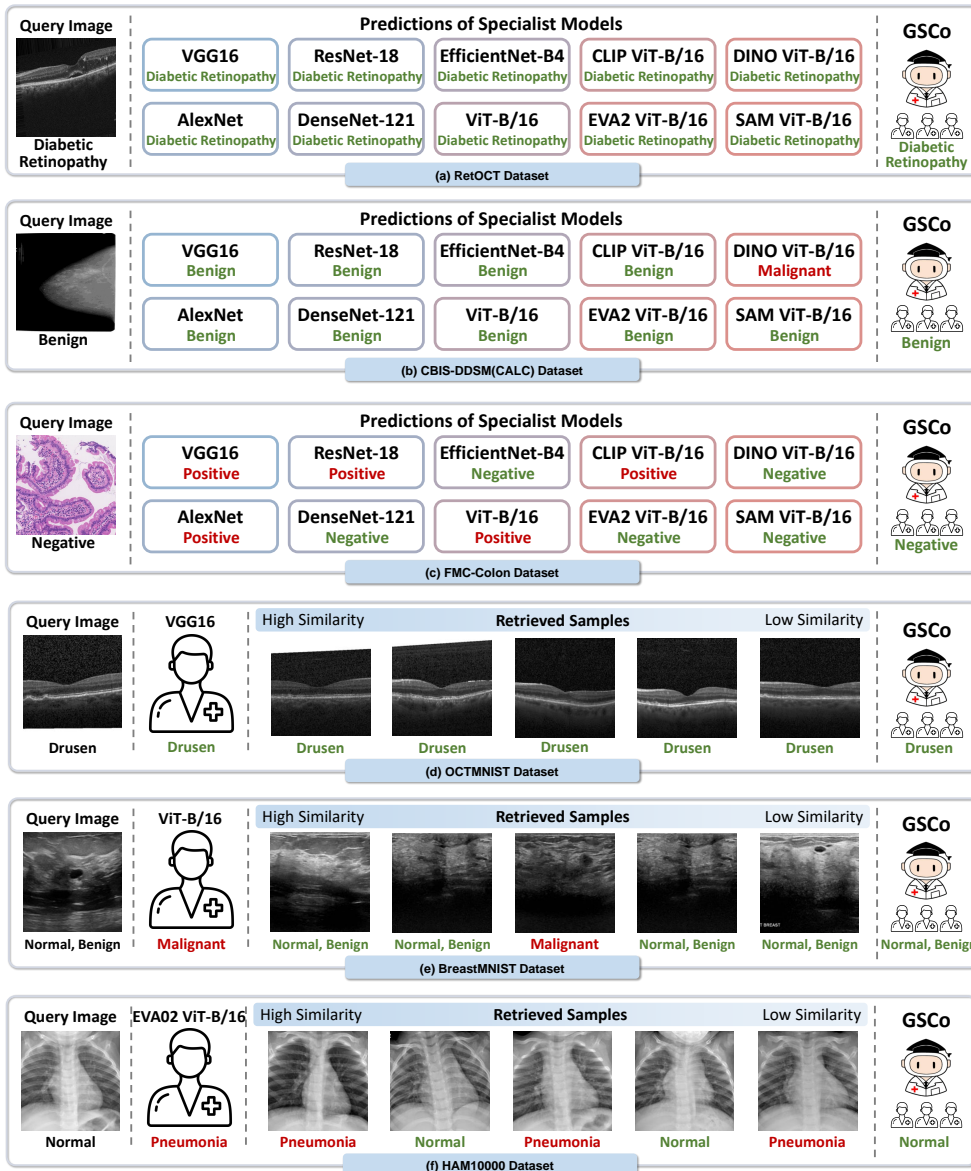


Fig. 5: Examples of mixture-of-expert diagnosis and retrieval-augmented diagnosis on downstream medical image diagnosis datasets. (a)-(c): Examples of mixture-of-expert diagnosis. Query image and its label, predictions of specialist models, and prediction of GSCo are listed. (d)-(e): Examples of retrieval-augmented diagnosis. Query image and its label, best specialist model and its prediction, top-5 retrieved similar images and their labels, and prediction of GSCo are listed. **Green** indicates the correct results while **Red** indicates the erroneous results. More examples are presented in **Extended Data Figures A2 and A1**.

of specialist models make correct predictions, thereby providing MedDr with effective guidance to derive accurate diagnoses. Secondly, we note that even if the aggregating results fail to offer correct reference, MedDr can arrive at the correct diagnoses as well. For example, on the FMC-Colon dataset (**Fig. 5 (c)**), half of the specialist models predict “Positive”, while the other half provide opposite results. While the naive “Voting” strategy fails in such a dilemma, MedDr generates the correct result “Negative”. These observations validate the superiority of MedDr and the efficacy of the proposed MoED. MedDr not only leverages the reference diagnoses provided by the specialist models but also utilizes its inherent knowledge to make the final decision. MoED represents an effective collaboration that integrates the strengths of both the Generalist and specialist models, thereby enhancing diagnostic accuracy.

Fig. 5(d)-(f) and **Extended Data Fig. A1** present examples of the RAD on downstream datasets covering a broad range of modalities. Firstly, we delve into the effectiveness of the retrieval strategy. As illustrated in **Fig. 5 (d)** and **Extended Data Fig. A1 (e)**, the retrieved images share the same label as the query image, thereby serving as reliable references. Notably, although the specialist may render an incorrect diagnosis as a predictor, the majority of images retrieved still provide accurate diagnostic information, demonstrating the specialist’s robust capability as a retriever. For instance, in **Fig. 5 (e)**, the specialist model predicts the “Malignant” while most of the retrieved samples are “Normal, Benign”. These observations suggest that, in most cases, the retrieved samples can offer accurate guidance for MedDr, thereby validating the precision and robustness of the retrieval strategy. Secondly, we explore the efficacy of RAD. In most cases of **Fig. 5(d)-(f)** and **Extended Data Fig. A1**, the retrieved samples provide correct guidance. Meanwhile, we observe that even if the predictions from the specialist model and the retrieved items contain distracting information, MedDr can still make an accurate diagnosis based on its inherent disease diagnosis capability. For example, as shown in **Fig. 5 (f)**, while most retrieved images are “Pneumonia” and therefore provide erroneous guidance, MedDr successfully derive the “Normal” diagnosis. These findings underscore that MedDr adeptly harnesses not only the external knowledge provided by the retrieved samples but also its inherent diagnostic capabilities, thereby demonstrating the effectiveness of the proposed RAD approach.

Ablation Study

In this section, we delve into the ablation study of the proposed MoED and RAD mechanisms. We perform experiments on nine medical image diagnosis datasets encompassing various medical modalities and tasks. **Extended Data Table A7** presents the experimental results. For binary classification, accuracy is reported. Otherwise, the Macro-F1 score is reported. Both MoED and RAD demonstrate consistent performance improvements for MedDr, achieving average enhancements of 0.2030 and 0.2065, respectively. Compared with MoED, RAD exhibits superior performance, which can be attributed to its utilization of not only domain-specific knowledge from specialists but also information from the training database, thereby offering MedDr more reliable references.

To further assess the effectiveness and generalizability of RAD, we conducted experiments on broader types of downstream tasks. In visual question answering and medical report generation tasks, developing a specialist model that consistently outperforms a GFM can be particularly challenging. If specialist models underperform, they may fail to offer reliable guidance to the GFM, which could lead to a decline in overall performance. Therefore, in the following experiments, we adopt the vision encoder of MedDr as the retriever. For medical image diagnosis tasks, following previous practice, we retrieve the labels of the five most similar cases. In visual question answering and medical report generation tasks, we retrieve the most similar images and then incorporate their corresponding annotations into the input. Additionally, we also introduce Med-Flamingo [Moor et al \(2023b\)](#) as a baseline model, which showcases impressive few-shot learning ability.

Extended Data Table A9 presents the results of medical image diagnosis, visual question answering, and medical report generation tasks. The “voting” column reflects the outcomes derived from a voting mechanism based on the labels of the retrieved samples. For medical report generation, we take the top-1 retrieved report as the “voting” results. Notably, both Med-Flamingo and MedDr exhibit significant and consistent improvements across most datasets and tasks, underscoring the generalizability of RAD. However, Med-Flamingo’s performance is upper-bounded by “voting”, indicating its heavy reliance on retrieved results for final diagnoses without adequately considering the image content. For instance, in the medical report generation task, Med-Flamingo often tends to directly rephrase or even replicate the retrieved samples with minimal modification. In contrast, MedDr consistently surpasses the “Voting” results across most downstream datasets, indicating that MedDr not only considers the retrieved results but also leverages its intrinsic knowledge for diagnosing the test images. Experiments validate the effectiveness of RAD, which can still enhance the capabilities of the GFM even in the absence of specialists, thereby boarding its application scenarios.

3 Discussion

To the best of our knowledge, we are the first to investigate the synergy between the GFM and specialist models. Concretely, we propose a collaborative framework Generalist-Specialist Collaboration (GSCo), to leverage the generalist’s in-context

learning abilities alongside the specialists’ domain-specific knowledge. GSCo consists of two stages, namely the construction of GFM and specialists, and collaborative inference on downstream tasks. In the construction stage, we first develop MedDr, the largest open-source GFM tailored for medicine, capable of handling a wide range of medical tasks and modalities. MedDr also exhibits remarkable proficiency in both instruction-following and in-context learning, providing a solid foundation for cooperation with specialist models. Meanwhile, a series of lightweight specialists are tailored for specific downstream tasks with low computational overhead. In the collaborative inference stage, Mixture-of-Expert Diagnosis (MoED) and Retrieval-Augmented Diagnosis (RAD) are proposed as the core mechanisms of the cooperation. MoED integrates predictions from specialists as reference diagnoses, while RAD employs these models to retrieve similar cases, collectively providing MedDr with in-context information to facilitate medical image analysis. To comprehensively evaluate MedDr and GSCo, we curate the largest benchmark in medical GFM, which consists of 28 datasets and about 250K testing samples, encompassing diverse medical modalities and tasks. Extensive qualitative and quantitative experiments highlight the following perspectives of our study.

MedDr excels in understanding and analysis. Compared with previous methods [Chen et al \(2023\)](#); [Li et al \(2024\)](#); [Moor et al \(2023b\)](#); [Wu et al \(2023b\)](#); [Tu et al \(2024\)](#), MedDr exhibits significant advantages in two key aspects. Firstly, as a generalist foundation model, MedDr demonstrates remarkable generalizability in medical image analysis, enabling it to process a broader scope of medical modalities, including radiology, pathology, dermatology, ophthalmology, and gastroenterology, and achieving state-of-the-art performance across various tasks, such as visual question answering, medical report generation, and medical image diagnosis. Secondly, MedDr showcases exceptional capabilities in instruction following and in-context learning. This enhances the model’s flexibility in handling different tasks and leveraging external knowledge, providing a solid foundation for effective collaboration with specialist models. These advantages can be attributed to our meticulously curated training corpus and the larger scale of MedDr. Concretely, the training corpus incorporates over 2 million samples across five distinct task types, thereby broadening the scope of MedDr. Additionally, with 40 billion parameters, MedDr surpasses previous models, endowing it with superior inherent capabilities. In the future, we plan to incorporate more diverse training corpora as well as a larger foundation model.

Instruction following and in-context learning enables the Generalist-Specialist Collaboration. In most previous methods [Chen et al \(2023\)](#); [Li et al \(2024\)](#); [Moor et al \(2023b\)](#); [Wu et al \(2023b\)](#); [Tu et al \(2024\)](#); [Zhang et al \(2024\)](#); [Yang et al \(2023\)](#), both GFMs and specialist models independently handle the downstream tasks with their inherent capabilities. GFMs are renowned for their generalizability and flexibility, enabling them to perform a variety of medical tasks across different modalities using a single model. In contrast, specialist models are esteemed for their precision and efficiency, achieving satisfactory performance by tailoring them to specific downstream tasks with low computational consumption. This work aims to explore the collaboration between generalist and specialist models, wherein instruction following and in-context learning, which previous methods overlooked, act as essential links

that facilitate their integration. Experimental results demonstrate that with exceptional instruction following and in-context learning capabilities, MedDr can effectively collaborate with specialist models and achieve SOTA performance on downstream tasks.

GSCo presents a novel paradigm in the clinical application of GFM and specialists. In clinical practice, collaboration among healthcare professionals is not only common but also essential. This study illustrates that through the synergistic collaboration between the GFM and specialist models, we can achieve superior performance on downstream tasks. GSCo presents a new paradigm in the clinical application of both GFM and specialists. Specifically, when confronted with out-of-domain tasks or data, rather than investing substantial resources to fine-tune the GFM, we can efficiently adapt lightweight specialist models with minimal resource expenditure. Additionally, due to the stringent privacy regulations governing most medical data, including Protected Health Information (PHI), directly fine-tuning the GFM on data from multiple sources is often impractical. Instead, under GSCo, we can integrate the knowledge from these private datasets by training the separate specialist models within their institutions independently, thereby safeguarding the confidentiality of medical data.

Mixture-of-expert diagnosis and retrieval-augmented diagnosis are effective collaboration strategies between the generalist and specialist models. In this study, we propose two mechanisms for providing MedDr with the guidance of the specialists, namely mixture-of-expert diagnosis and retrieval-augmented diagnosis. Mixture-of-expert diagnosis leverages the specialist model’s predictions as references, while retrieval-augmented diagnosis treats the specialist model as a retriever to access relevant information in the training dataset. In such collaboration, the roles of MedDr and specialists are distinct. The specialist model plays a pivotal role in equipping the GFM with reference guidance to enhance its generalization capabilities, particularly for out-of-domain tasks. Meanwhile, MedDr functions as a decision-maker with a wealth of medical knowledge. Through extensive experiments, it has been demonstrated that these mechanisms enable the GFM to benefit from the specialist model’s expertise, resulting in a robust and generalizable AI for medicine.

Limitations and further directions. Despite the advancements, the experimental results also reveal existing limitations, providing clear directions for future enhancements and research. Firstly, while GSCo has demonstrated satisfactory performance across various public datasets, further exploration of its application in clinical practice is necessary to substantiate the superiority of the methodology. Secondly, multimodal retrieval strategies should be further explored. GSCo has showcased the significant potential of retrieval-augmented generation in medical image analysis. However, the current vision-based retrieval method still struggles to ensure the accuracy of the retrieved samples. Lastly, diverse collaborative paradigms require exploration. While GSCo has validated the effectiveness of collaboration, we anticipate observing more interaction patterns between generalists and specialists. For instance, incorporating Chain of Thought (CoT) [Wei et al \(2022\)](#) could be a viable approach to facilitating collaboration between generalists and specialists.

4 Method

Construction of GFM and Specialists

Diagnosis-Guided Bootstrapping and Medical Image Description dataset

In this section, we introduce the proposed Diagnosis-Guided Bootstrapping (DGB) and Medical Image Description (DES) datasets. To leverage the abundant medical image diagnosis datasets, we first present the DGB dataset. Previous methods [Li et al \(2024\)](#); [Wu et al \(2023b\)](#) have constructed instruction-tuning datasets primarily derived from PubMed research articles, to alleviate the scarcity of vision-language data in the medical domain. Although these strategies have successfully assembled large-scale training corpora, they present two significant limitations. Firstly, they rely solely on textual information, neglecting visual elements, which may lead to inconsistencies in descriptions. Secondly, the content of research articles might lack reliability and accuracy, thereby introducing noise into the training corpus.

In contrast, we propose to generate the instruction tuning dataset based on medical image diagnosis datasets, exploiting multi-modal information and human-verified annotations. As shown in [Fig. 7 \(a\)](#), we observe that GFMs in the general domain [Chen et al \(2023\)](#); [Liu et al \(2023\)](#) exhibit a comprehensive understanding of disease-related information and associated symptoms, owing to extensive training on diverse corpora. Nonetheless, these models encounter difficulties in correlating this knowledge with specific medical images, leading to inaccurate diagnostic predictions. Conversely, when provided with specific disease and modality information alongside the given image, the GFM in the general domain is capable of generating high-quality medical reports with accurate diagnoses. For example, [Fig. 7 \(b\)](#) presents a generated report on “ulcerative colitis”, where findings enumerate the observations in the image and the impression encapsulates the conclusion.

Motivated by the above observations, we propose a diagnosis-guided bootstrapping strategy that leverages both visual and textual information to construct the instruction-tuning dataset. Specifically, we format the instruction as shown in [Fig. 6](#). We provide the model with information about the modality and disease of the medical image and require it to generate a detailed report.

Prompt for Diagnosis-Guided Bootstrapping
You are a helpful medical assistant. Your task is medical report generation. You are given a {Modality} image, and the diagnosis is {Disease} . You need to provide a medical report consisting of findings and impressions.

Fig. 6: Prompt for diagnosis-guided bootstrapping. **{Modality}** and **{Disease}** are placeholders for the corresponding information.

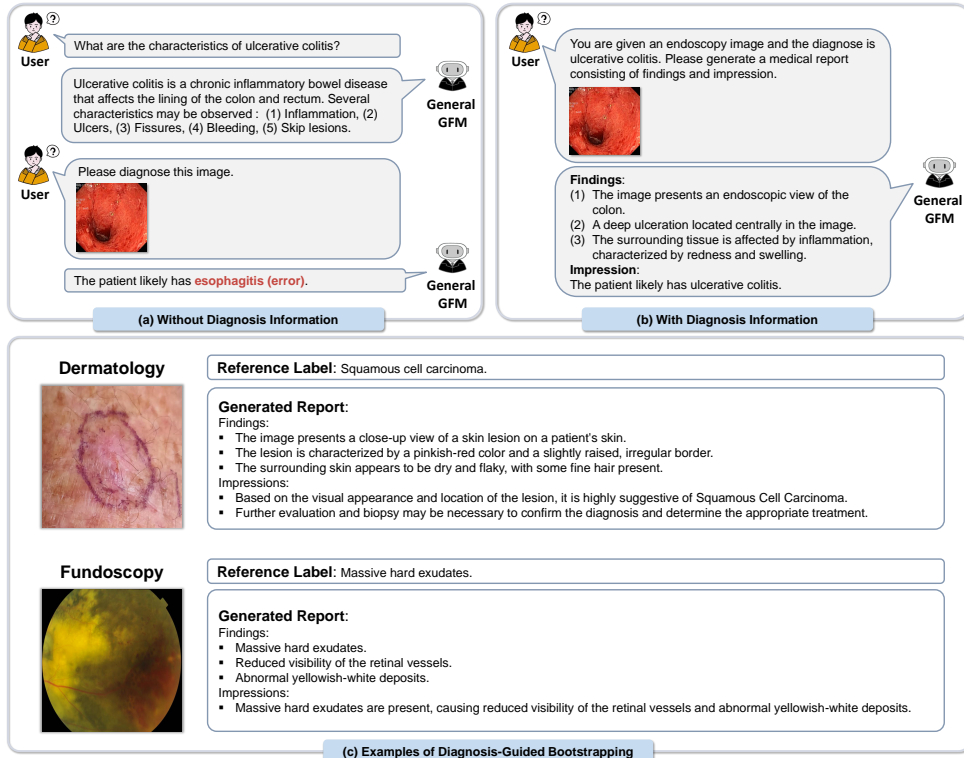


Fig. 7: (a) The generalist foundation model in the general domain has the knowledge about diseases but it is challenging to correlate the knowledge with querying images, leading to **incorrect diagnosis**. (b) Guided by the correct diagnosis, the generalist foundation model generates a detailed medical report consisting of findings and impressions. (c) Examples of the generated reports across different medical modalities.

In contrast to previous works [Li et al \(2024\)](#); [Wu et al \(2023b\)](#), which generated data from textual information only, our approach offers two prominent advantages. Firstly, it facilitates the utilization of numerous human-verified label-level annotated datasets in medicine. Secondly, incorporating both visual and textual information ensures that the generated information remains pertinent to the accompanying images. Following this method, we build the DGB dataset encompassing diverse medical image modalities.

Meanwhile, to augment the diversity of our training data, we present the Medical Image Description (DES) datasets. Specifically, we collect the image-based case studies from OpenI [Demner-Fushman et al \(2012\)](#) and then employ the GFM [Chen et al \(2023\)](#) to write a description of the image from a medical perspective, integrating both the image and associated textual information. Additionally, we also exclude the details that are not inferable directly from the image, such as the patient’s name or age, to maintain focus on diagnostically relevant visual features.

Medical Instruction Tuning

To advance the multifaceted capabilities of the GFM, following previous methods Li et al (2024); Wu et al (2023b); Moor et al (2023b), we incorporate visual question answering He et al (2020); Lau et al (2018); Liu et al (2021); Zhang et al (2023b); Wu et al (2023b) and medical report generation Johnson et al (2019); Demner-Fushman et al (2016) datasets into our training corpus. Overall, as depicted in **Fig. 1 (b)**, our training corpus encompasses five different types of items: medical image diagnosis (CLS), medical report generation (MRG), visual question answering (VQA), diagnosis-guided bootstrapping (DGB), and medical image description (DES). We meticulously crafted the prompt template for each type, as listed in **Extended Data Fig. A3**. More detailed information about the training datasets is presented in **Section 4**. The language modeling loss is utilized as the loss function to train the model.

Collaborative Inference on Downstream Tasks

Mixture-of-Expert Diagnosis

When addressing a specific downstream task, training a lightweight specialist model can often be more practical than utilizing GFMs. This advantage is primarily due to the significantly lower training overhead while still achieving satisfactory performance. In this study, we investigate the collaborative potential between generalist and specialist models, to enhance outcomes on downstream tasks.

As shown in **Fig. 8**, we select several lightweight models and train them on the downstream dataset, designating these as specialist models. Unlike the GFM, these specialist models are tailored to specific downstream tasks, yielding superior performance on these tasks due to expert knowledge. During the inference phase, we first input the testing image into the specialist models and utilize their predictions as a guiding reference, which is subsequently incorporated into the instruction. MedDr integrates both the testing image and the reference predictions to render the final diagnosis.

Retrieval-Augmented Diagnosis

GFMs have demonstrated significant capabilities but still face challenges when encountering out-of-domain data Chen et al (2023); Van Veen et al (2023). To exploit the training corpus exhaustively and enhance the capability on out-of-domain datasets, we propose a collaborative mechanism, Retrieval-Augmented Diagnosis.

Fig. 9 illustrates the proposed method, where the database is built on the training data across multiple medical tasks and modalities. Concretely, to build the database, given an image-text pair, we encode the image by an embedding model and take this visual embedding as the key while the text is the value. During the inference time, we first employ the embedding model to encode the test image. Then, the visual embedding of the test image is used to query the database by calculating the cosine similarity between the query and keys. The top- k most similar items from the database are retrieved, and then their meta information is incorporated into the instruction as additional textual clues to help the model make medical decisions.

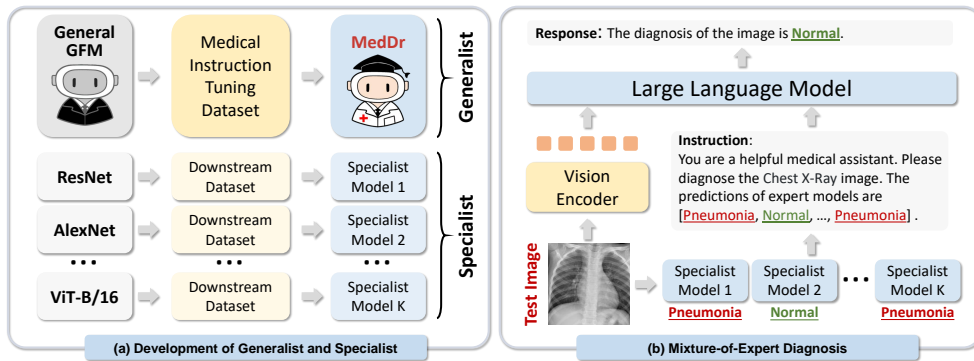


Fig. 8: Mixture-of-Expert Diagnosis. (a) MedDr is a generalist foundation model trained on a large-scale medical instruction tuning dataset. The specialist models are lightweight models trained on specific downstream datasets, requiring much lower training and inference consumption. (b) During the inference on downstream tasks, the test image is fed into the specialist models first and their responses will act as the reference for MedDr.

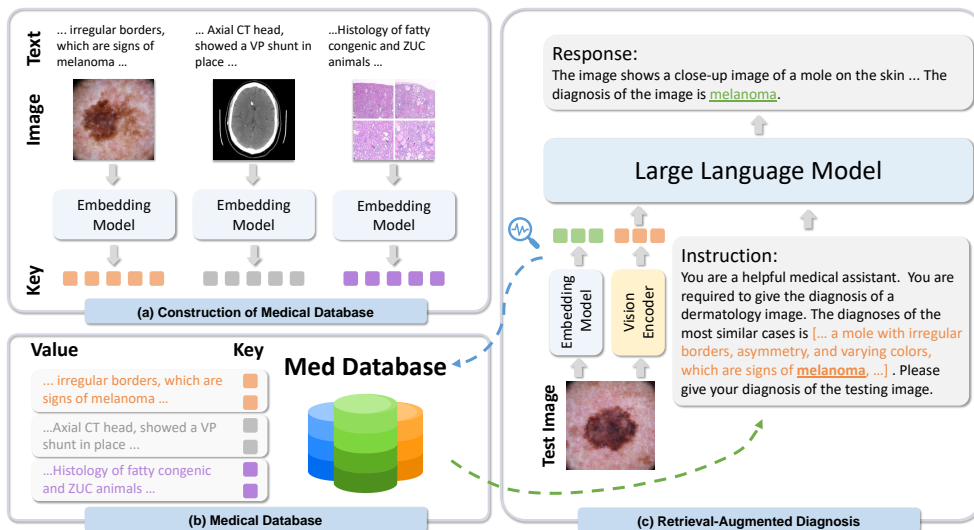


Fig. 9: Retrieval-Augmented Diagnosis. (a) An embedding model is employed to extract visual embeddings of images in medical image-text pairs. (b) Each database entry comprises meta-information along with its indexed embedding. (c) During the inference, we take the embedding of the test image to query the database and retrieve similar samples. The information from the retrieved samples is integrated into the instruction as contextual information. Both the test image and the instruction are then fed into MedDr.

In this study, we first explore utilizing the specialist model as the retriever. After fine-tuning on the specific downstream dataset, this specialist model is capable of generating more discriminative embeddings, thereby enhancing retrieval accuracy. Furthermore, we also explore the application of the vision encoder from MedDr as the retriever, which showcases two advantages. First, it effectively eliminates the need for an additional embedding module, which in turn reduces associated computational costs. By leveraging the vision encoder from MedDr as the embedding module, we can directly use the intermediate results as embeddings for queries during inference without incurring any extra overhead. Second, this approach is applicable to a wider array of scenarios, particularly in situations where acquiring a qualified specialist model poses challenges.

Implementation Details

In this work, we employ InternVL [Chen et al \(2023\)](#), a state-of-the-art GFM in the general domain, as our foundation model, which contains about 40B parameters, consisting of a 6B vision encoder and a 34B large language model. The input image is resized to 448×448 pixels. The model is fine-tuned on both collected and generated data. The number of training samples is about 2M. Please refer to **Section 4** for detailed information about the training dataset and instruction prompt. The instruction tuning recipe follows the suggestions provided by InternVL. We fix all parameters except for the LoRA component, which is composed of approximately 0.1B parameters, accounting for 0.4% of the total parameters. Meanwhile, we also leverage DeepSpeed ZeRO Stage 3 [Rajbhandari et al \(2021\)](#) to optimize the training procedure. The model is trained on 16 NVIDIA H800 GPUs for two epochs within 72 hours. The specialist models are trained on a single NVIDIA 4090 GPU and the corresponding recipe is presented in **Extended Data Table A13**.

State-of-the-art Generalist and Specialist Models

In this study, we select 4 open-source models in both the general and medical domains as the baseline GFMs.

- **RadFM** [Wu et al \(2023b\)](#) mainly focuses on the radiology modality. It consists of a 3D ViT as the vision backbone and PMC-LLaMA-13B [Wu et al \(2023a\)](#) as the LLM. The model is first trained on 16M noisy pre-training data and then fine-tuned on 3M in-domain data.
- **LLaVA-Med** [Li et al \(2024\)](#) is built on the pre-trained LLaVA [Liu et al \(2023\)](#). It is fine-tuned on about 600K concept alignment samples and 60K instruction tuning samples in one day with 8 A100 GPUs.
- **Med-Flamingo** [Moor et al \(2023b\)](#) is developed based on OpenFlamingo-9B [Awadalla et al \(2023\)](#), which can handle multiple images interleaved with texts. It is trained on large-scale interleaved datasets based on medical textbooks and the PMC-OA dataset [Lin et al \(2023\)](#).
- **InternVL** [Chen et al \(2023\)](#) is one of the most powerful open-source large-scale vision-language models in the general domain. It obtains SOTA performance on multi-modal tasks in the general domain.

For these GFMs, we reproduce the above models based on their open-source checkpoint and evaluate the model using the same test data. The test prompt is set up according to their official implementations (**Extended Data Table A16**).

For the choice of the specialist models, following [Doerrich et al \(2024\)](#), we select ten representative computer vision models and train them on the specific downstream datasets:

- **VGG16** [Simonyan and Zisserman \(2014\)](#) is a convolution-based model. It consists of 16 layers and is known for its simplicity and effectiveness.
- **AlexNet** [Krizhevsky et al \(2012\)](#) is a convolution-based model. It won the ImageNet Large Scale Visual Recognition Challenge (ILSVRC) in 2012 and popularized the use of convolutional neural networks (CNNs).
- **ResNet-18** [He et al \(2016\)](#) is a convolution-based model. It introduced residual connections that allow gradients to flow directly through the network, enabling the training of very deep networks.
- **DenseNet-121** [Huang et al \(2017\)](#) is a convolution-based model. It encourages feature reuse by connecting each layer to every other layer in a feed-forward fashion.
- **EfficientNet-B4** [Tan and Le \(2019\)](#) is a convolution-based model. It balances depth, width, and resolution to achieve high performance with fewer parameters. It is efficient in terms of both accuracy and computation.
- **ViT-B/16** [Dosovitskiy et al \(2021\)](#) is a Transformer-based model. It applies the Transformer architecture to image data, achieving competitive results on various vision tasks.
- **CLIP ViT-B/16** [Radford et al \(2021\)](#) is a Transformer-based model. It learns to associate images and text in a joint embedding space, enabling zero-shot classification and other multimodal tasks.
- **EVA-02 ViT-B/16** [Fang et al \(2023\)](#) is a Transformer-based model. It improves the training techniques for CLIP at scale and achieves superior performance with significantly smaller training costs.
- **DINO ViT-B/16** [Caron et al \(2021\)](#) is a Transformer-based model. It leverages clustering and momentum encoders and achieves strong performance without using labeled data.
- **SAM ViT-B/16** [Kirillov et al \(2023\)](#) is a Transformer-based model, which is designed to be a general-purpose model for image segmentation, capable of segmenting any object in an image with minimal user input.

The details of these specialist models are listed in **Extended Data Table A12**. The fine-tuning recipe on the downstream dataset is shown in **Extended Data Table A13**. Compared with the GFMs, these models have much fewer parameters and can be trained on consumer-level hardware, like NVIDIA 4090 GPU.

Training Dataset

In this section, we introduce the training dataset in detail and **Extended Data Fig. A3** presents the prompt template for each type of dataset.

Visual Question Answering Datasets

- **SLAKE** Liu et al (2021) is a bilingual radiology VQA dataset comprising 642 images and 14K questions. We only use the English part of the training split, which consists of 4,919 question-answer pairs.
- **VQA-RAD** Lau et al (2018) is a manually constructed dataset where clinicians asked naturally occurring questions of radiology images and provided reference answers. Following the official split, we use 3,064 question-answer pairs of the training set.
- **Path-VQA** He et al (2020) consists of 32,799 open-ended questions from 4,998 pathology images, where each question is manually checked to ensure correctness. Following the official split, we use 19,755 question-answer pairs of the training set.
- **PMC-VQA** Zhang et al (2023b) is a large-scale medical visual question-answering dataset built from image-text pairs from PubMed Central, covering broader medical image modalities. Following the official split, we use 152,603 question-answer pairs of the training set.
- **PMC-CaseReport** Wu et al (2023b) is an auto-generated visual question-answering dataset based on the case report papers in the PMC-Inline dataset. Following the official split, we use 254,105 question-answer pairs of the training set.

Medical Report Generation Datasets

- **MIMIC-CXR** Johnson et al (2019) presents 371,920 chest X-rays associated with 227,943 imaging studies from 65,079 patients. Following RadFM Wu et al (2023b) and R2Gen Chen et al (2020), we use 337,292 cases for training.
- **IU-Xray** Demner-Fushman et al (2016) is a set of chest X-ray images paired with their corresponding diagnostic reports. The dataset contains 7,470 pairs of images and reports. Following R2Gen Chen et al (2020), we use 4,730 cases from the training split.

Medical Image Diagnosis Datasets

- **VinDr-SpineXR** Nguyen et al (2021) is a large annotated medical image dataset for spinal lesion detection and classification from radiographs. Following RadFM Chen et al (2020), we use 6,129 samples for training.
- **VinDr-PCXR** Pham et al (2022) is an open-source large-scale pediatric chest X-ray dataset for the interpretation of common thoracic diseases. Following RadFM Chen et al (2020), we use 4,585 samples for training.
- **VinDr-Mammo** Nguyen et al (2023) is a large-scale benchmark dataset for computer-aided detection and diagnosis in full-field digital mammography. Following RadFM Chen et al (2020), we use 6,047 samples for training.
- **VinDr-CXR** Nguyen et al (2020) is an open large-scale dataset of chest X-rays with radiologist’s annotations. The training set contains 15,000 scans, and 3 radiologists independently label each image. Following the official split, we use 45,000 samples for training.

- **CheXpert** [Irvin et al \(2019\)](#) is a large public dataset for chest radiograph interpretation, consisting of 224,316 chest radiographs of 65,240 patients. Following the official split, we use 223,414 samples for training.
- **ChestX-ray14** [Wang et al \(2017\)](#) is a medical imaging dataset which comprises 112,120 frontal-view X-ray images of 30,805 patients with the text-mined fourteen common disease labels. Following the official split, we use 86,524 samples for training.
- **PCam200** [Kawai et al \(2023\)](#) is a public pathological H&E image dataset made in the same manner from Camelyon2016 challenge dataset [Bejnordi et al \(2017\)](#). Following the official split, we use 28,539 samples for training.
- **PAD-UFES-20** [Pacheco et al \(2020\)](#) is a dermatology classification dataset consisting of 2,298 images for six different diagnostics. We use all of the 2,298 samples for training.
- **DermNet** [Goel \(2020\)](#) consists of dermatology images of 23 types of skin diseases taken from DermNet. Following the official split, we use 15,557 samples for training.
- **HAM10000** [Tschandl et al \(2018\)](#) is a large collection of multi-source dermatoscopic images of pigmented lesions. Following the official split, we use 10,015 samples for training.
- **ISIC2020** [Rotemberg et al \(2021\)](#) is a dataset of the SIIM-ISIC Melanoma Classification Challenge 2020. The dataset contains 33,126 dermoscopic training images of unique benign and malignant skin lesions from over 2,000 patients. Following the official split, we use 33,126 samples for training.
- **Kvasir** [Pogorelov et al \(2017\)](#) is a multi-class image dataset for computer-aided gastrointestinal disease detection. Following the official split, we use 8,000 samples for training.
- **Kvasir Capsule** [Smedsrud et al \(2021\)](#) is an endoscopy dataset consisting of 47,238 images with annotations of anatomical landmarks and pathological and normal findings. Following the official split, we use 47,238 samples for training.
- **WCE** [Montalbo \(2022\)](#) is a curated colon disease dataset based on Kvasir [Pogorelov et al \(2017\)](#) and ETIS-Larib-Polyp DB [Silva et al \(2014\)](#). Following the official split, we use 3,200 samples for training.
- **GastroVision** [Jha et al \(2023\)](#) is a multi-center open-access gastrointestinal (GI) endoscopy dataset that includes different anatomical landmarks, pathological abnormalities, polyp removal cases, and normal findings from the GI tract. We use all of the 8,000 samples for training.
- **ODIR** [Li et al \(2021\)](#) is a structured ophthalmic database of 5,000 patients with age, color fundus photographs from left and right eyes, and doctors' diagnostic keywords. Following the official split, we use 6,392 samples for training.
- **Fundus1000** [Cen et al \(2021\)](#) contains 1,000 fundus images with 39 categories. We use all of the 1,000 samples for training.
- **RFMiD2.0** [Panchal et al \(2023\)](#) is a multi-label dataset including around 860 retinal fundus images annotated by three eye specialists. Following the official split, we use 455 samples for training.
- **Retinal OCT-C8** [Subramanian et al \(2022\)](#) is a large-scale dataset for ophthalmic research containing 24,000 optical coherence tomography (OCT) images that are

organized into eight categories. Following the official split, we use 18,000 samples for training.

- **UltraBreast** is a private breast ultrasound dataset that contains 45,896 cases that are labeled benign or malignant.

Synthetic Datasets

Diagnosis-Guided Bootstrapping Dataset. As introduced in Section 4, we constructed a large-scale medical report dataset across diverse medical modalities. Concretely, we generate 196,760 samples in total based on the VinDr-SpineXR [Nguyen et al \(2021\)](#), VinDr-PCXR [Pham et al \(2022\)](#), VinDr-Mammo [Nguyen et al \(2023\)](#), VinDr-CXR [Nguyen et al \(2020\)](#), ChestX-ray14 [Wang et al \(2017\)](#), PAD-UFES-20 [Pacheco et al \(2020\)](#), Dermnet [Goel \(2020\)](#), Kvasir [Pogorelov et al \(2017\)](#), WCE [Montalbo \(2022\)](#), Kvasir Capsule [Smedsrud et al \(2021\)](#), ODIR [Li et al \(2021\)](#), Fundus1000 [Cen et al \(2021\)](#) and RFMiD2.0 [Panchal et al \(2023\)](#) datasets.

Medical Image Description Dataset. To augment the diversity of our training data, we also collected 245,371 image-based case studies from OpenI [Demner-Fushman et al \(2012\)](#). We summarize the title of the case and the image caption based on the image by InternVL [Chen et al \(2023\)](#) and obtain high-quality images and corresponding text summaries.

Out-of-Domain Benchmark Dataset

Visual Question Answering Datasets

- **VQA-Med** [Ben Abacha et al \(2019\)](#) focuses on radiology images and consists of four main categories of questions: modality, plane, organ system, and abnormality. Following the official split, we use 500 items for testing.
- **OmniMedVQA** [Hu et al \(2024\)](#) is a large-scale comprehensive evaluation benchmark dataset for the medical GFMs. Due to the overlap with our training data, we exclude some data to prevent data leakage and only use the Disease Diagnosis subset. The total number of the testing samples is 51,977.

Medical Image Diagnosis Datasets

- **PneumoniaMNIST** [Yang et al \(2023\)](#) is a binary classification dataset about chest X-ray. Following the official split, we use 624 items for testing.
- **BreastMNIST** [Yang et al \(2023\)](#) is a binary classification dataset of breast ultrasound. Following the official split, we use 156 samples for testing.
- **OrganAMNIST** [Yang et al \(2023\)](#) is a multi-class classification dataset of abdominal CT. Following the official split, we use 17,778 items for testing.
- **PathMNIST** [Yang et al \(2023\)](#) is a multi-class classification dataset of colon pathology. Following the official split, we use 7,180 items for testing.
- **OCTMNIST** [Yang et al \(2023\)](#) a multi-class classification dataset of retinal OCT. Following the official split, we use 1,000 items for testing.
- **ChestMNIST** [Yang et al \(2023\)](#) is a multi-label dataset of chest X-ray. Following the official split, we use 22,433 samples for testing.

- **CBIS-DDSM** [Sawyer-Lee et al \(2016\)](#) contains images for screening mammography. The original dataset contains images of cases with three conditions of breast cancer: BENIGN, BENIGN_WITHOUT_CALLBACK, and MALIGNANT. Due to the insufficient information in the text to discriminate between BENIGN and BENIGN_WITHOUT_CALLBACK, we formulate it as a binary classification task. Following the official split, we use 326 samples from the CALC subset and 378 samples from MASS for testing.
- **FMC-Colon** [Wang et al \(2023\)](#) is a pathological tumor tissue classification dataset and requests the model to determine whether the sample is positive or negative. Following the official split, we use 4,355 samples for testing.
- **FMC-Endo** [Wang et al \(2023\)](#) is a colonoscopy lesion classification dataset and consists of four different lesion types. Following the official split, we use 2,055 samples for testing.
- **FMC-Chest** [Wang et al \(2023\)](#) is a thoracic disease screening dataset and covers 19 common thoracic abnormalities. Following the official split, we use 2,708 samples for testing.
- **Derm7pt** [Kawahara et al \(2018\)](#) is a dataset for evaluating computerized image-based prediction of the 7-point skin lesion malignancy checklist. Following the official split, we use 395 samples for testing.
- **BRSET** [Nakayama et al \(2023\)](#) is a multi-labeled ophthalmological dataset designed to improve scientific community development and validate machine learning models. We randomly divided the dataset into training and testing splits with an 8:2 ratio. The number of testing samples is 3,254.

Evaluation Metrics

Medical Image Diagnosis

For the medical image diagnosis datasets, accuracy and F1-Score are exploited for evaluation. Accuracy is calculated as

$$\text{Accuracy} = \frac{1}{N} \sum_i^N 1(y_i = \hat{y}_i),$$

where y is a tensor of target values, and \hat{y} is a tensor of predictions. F1-Score is defined based on recall and precision as follows,

$$\begin{aligned} \text{Recall} &= \frac{\text{TP}}{\text{TP} + \text{FN}}, \\ \text{Precision} &= \frac{\text{TP}}{\text{TP} + \text{FP}}, \\ \text{F1-Score} &= 2 \cdot \frac{\text{Precision} * \text{Recall}}{\text{Precision} + \text{Recall}}, \end{aligned}$$

where TP and FP represent the number of true positives and false positives respectively. Especially, for multi-class and multi-label classification datasets, we calculate both Macro-F1 Score and Micro-F1 Score.

Visual Question Answering

For the dataset consisting of multiple choice questions [Hu et al \(2024\)](#), we calculate the accuracy. For other visual question answering datasets, following MultiMedEval [Royer et al \(2024\)](#), we first tokenize both prediction and answer and compute precision and recall. For close-ended questions, the prediction is correct if its recall is at least 0.5. For open-ended questions, the prediction is correct if its recall is at least 0.75. We report the accuracy of close-ended questions and the accuracy and recall of the open-ended questions. The overall F1-Score and recall are also reported. Additionally, following [Wu et al \(2023b\)](#), we compute the BLEU-1 score as follows:

$$\text{BLEU-1} = \text{BP} \cdot \exp \left(\sum_{n=1}^N w_n \cdot \log p_n \right),$$

where BP is the brevity penalty, p_n is the precision for n-grams, and w_n is the weight for n-gram precision. If the predicting result’s length c is greater than the reference length r , then $\text{BP} = 1$. If $c \leq r$, then $\text{BP} = \exp(1 - r/c)$. This ensures that a shorter predicting result is penalized to prevent the system from favoring overly concise output. Since there is only one type of n-gram, $w_1 = 1$. The brevity penalty (BP) is used to adjust the BLEU score based on the length of the candidate translation compared to the reference translation. It’s calculated as follows:

Medical Report Generation

For medical report generation tasks, we utilize common n-gram-based metrics such as BLEU-1, BLEU-4, ROUGE-1, ROUGE-L, and METEOR [Banerjee and Lavie \(2005\)](#). Here, ROUGE-1 is defined as follows,

$$\text{ROUGE-1} = \frac{|\text{Recall} \cap \text{Reference}|}{|\text{Reference}|},$$

where $|\text{Recall} \cap \text{Reference}|$ is the number of overlapping unigrams between the generated report and the reference report, whereas $|\text{Reference}|$ refers to the total number of unigrams in the reference text. ROUGR-L is defined as

$$\text{ROUGE-L} = \frac{F_{LCS}}{|\text{Reference}|},$$

where F_{LCS} represents the F1 score of the longest common subsequence.

The METEOR score is computed as:

$$\text{METEOR} = \frac{1}{m} \cdot \sum_{g \in \text{gold}} \max_{h \in \text{hyp}} \text{Precision}(g, h),$$

where m is the number of gold standard (reference) sentences, and $\text{Precision}(g, h)$ refers to the precision score between a specific gold standard sentence (g) and a hypothesis sentence (h) from the set of all gold standard sentences (gold) and the set of all hypothesis sentences (hyp).

Moreover, we evaluate F1-RadGraph, which measures the F1 score between entities extracted from the reference and generated reports using RadGraph Jain et al (????):

$$\text{F1-RadGraph} = 2 \cdot \frac{\text{Precision} \cdot \text{Recall}}{\text{Precision} + \text{Recall}}.$$

We also compute CheXbert vector similarity Yu et al (2023) using cosine similarity between the embedded reference and generated reports:

$$\text{Cosine Similarity} = \frac{A \cdot B}{\|A\| \|B\|},$$

where A and B are the vectors of the reference and generated reports, respectively.

Data availability

The datasets used for building the training dataset are listed in **Extended Data Table A14**, and the evaluation benchmark datasets are listed in **Extended Data Table A15**.

Code availability

The implementation of MedDr and GSCo framework will be available at <https://github.com/sunanhe/MedDr>. The weights of MedDr and specialist models will be available in https://huggingface.co/Sunanhe/MedDr_0401. The other public codes used in this study are listed in **Extended Data Table A16**.

Author contribution

S.H., Y.N., and H.C. conceived and designed the work. S.H., Y.N., contributed to the technical implementation and conducted experiments. S.H., Y.N., Zhixuan.C., Zhiyuan.C., H.W., S.Y., Y.W., and Y.X. contributed to the data acquisition and organization. L.L., H.X., X.L., M.W, Y.P, G.S, Z.X, X.W, Q.W., R.C.K.C, V.V, W.C.W.C., Y.Z, P.R., and K.Z. provided suggestions on the framework and experiments. All authors contributed to the drafting and revising of the manuscript. H.C. supervised the research.

Declarations

The authors have no conflicts of interest to declare.

Ethics declarations

This study has been reviewed and approved by the Human and Artefacts Research Ethics Committee (HAREC). The protocol number is HREP-2024-0212.

Acknowledgements

This work was supported by the Hong Kong Innovation and Technology Commission (Project No. MHP/002/22 and TCPD/17-9), HKUST 30 for 30 Research Initiative

Scheme, Cornell–HKUST Global Strategic Collaboration Awards, Asian Young Scientist Fellowship and the Research Grants Council of the Hong Kong (Project Reference Number: T45-401/22-N).

References

- Achiam J, Adler S, Agarwal S, et al (2023) Gpt-4 technical report. arXiv preprint arXiv:230308774
- Anil R, Dai AM, Firat O, et al (2023) Palm 2 technical report. arXiv preprint arXiv:230510403
- Antol S, Agrawal A, Lu J, et al (2015) Vqa: Visual question answering. In: Proceedings of the IEEE International Conference on Computer Vision (ICCV)
- Awadalla A, Gao I, Gardner J, et al (2023) Openflamingo: An open-source framework for training large autoregressive vision-language models. arXiv preprint arXiv:230801390
- Banerjee S, Lavie A (2005) Meteor: An automatic metric for mt evaluation with improved correlation with human judgments. In: Proceedings of the acl workshop on intrinsic and extrinsic evaluation measures for machine translation and/or summarization, pp 65–72
- Bejnordi BE, Veta M, Van Diest PJ, et al (2017) Diagnostic assessment of deep learning algorithms for detection of lymph node metastases in women with breast cancer. *Jama* 318(22):2199–2210
- Ben Abacha A, Hasan SA, Datla VV, et al (2019) Vqa-med: Overview of the medical visual question answering task at imageclef 2019. In: Working Notes of CLEF 2019, CEUR Workshop Proceedings, vol 2380. CEUR-WS.org, Lugano, Switzerland, URL https://ceur-ws.org/Vol-2380/paper_272.pdf
- Caron M, Touvron H, Misra I, et al (2021) Emerging properties in self-supervised vision transformers. In: Proceedings of the IEEE International Conference on Computer Vision (ICCV), pp 9650–9660
- Cen LP, Ji J, Lin JW, et al (2021) Automatic detection of 39 fundus diseases and conditions in retinal photographs using deep neural networks. *Nature communications* 12(1):4828
- Chen P, Ye J, Wang G, et al (2024a) Gmai-mmbench: A comprehensive multimodal evaluation benchmark towards general medical ai. arXiv preprint arXiv:240803361
- Chen Z, Song Y, Chang TH, et al (2020) Generating radiology reports via memory-driven transformer. In: Proceedings of the 2020 Conference on Empirical Methods in Natural Language Processing
- Chen Z, Wu J, Wang W, et al (2023) Internvl: Scaling up vision foundation models and aligning for generic visual-linguistic tasks. arXiv preprint arXiv:231214238

- Chen Z, Luo L, Bie Y, et al (2024b) Dia-llama: Towards large language model-driven ct report generation. arXiv preprint arXiv:240316386
- Demner-Fushman D, Antani S, Simpson M, et al (2012) Design and development of a multimodal biomedical information retrieval system. *Journal of Computing Science and Engineering* 6(2):168–177
- Demner-Fushman D, Kohli MD, Rosenman MB, et al (2016) Preparing a collection of radiology examinations for distribution and retrieval. *Journal of the American Medical Informatics Association* 23(2):304–310
- Deng J, Dong W, Socher R, et al (2009) Imagenet: A large-scale hierarchical image database. In: *Proceedings of the IEEE Conference on Computer Vision and Pattern Recognition (CVPR)*, Ieee, pp 248–255
- Doerrich S, Di Salvo F, Brockmann J, et al (2024) Rethinking model prototyping through the medmnist+ dataset collection. arXiv preprint arXiv:240415786
- Dosovitskiy A, Beyer L, Kolesnikov A, et al (2021) An image is worth 16x16 words: Transformers for image recognition at scale. In: *International Conference on Learning Representations*, URL <https://openreview.net/forum?id=YicbFdNTTy>
- Fang Y, Sun Q, Wang X, et al (2023) Eva-02: A visual representation for neon genesis. arXiv preprint arXiv:230311331
- Fedus W, Zoph B, Shazeer N (2022) Switch transformers: Scaling to trillion parameter models with simple and efficient sparsity. *Journal of Machine Learning Research* 23(120):1–39
- Goel S (2020) Dermnet. <https://www.kaggle.com/datasets/shubhamgoel27/dermnet>
- He K, Zhang X, Ren S, et al (2016) Deep residual learning for image recognition. In: *Proceedings of the IEEE Conference on Computer Vision and Pattern Recognition (CVPR)*, pp 770–778
- He X, Zhang Y, Mou L, et al (2020) Pathvqa: 30000+ questions for medical visual question answering. arXiv preprint arXiv:200310286
- Hu Y, Li T, Lu Q, et al (2024) Omnimedvqa: A new large-scale comprehensive evaluation benchmark for medical lvlm. arXiv preprint arXiv:240209181
- Huang G, Liu Z, Van Der Maaten L, et al (2017) Densely connected convolutional networks. In: *Proceedings of the IEEE Conference on Computer Vision and Pattern Recognition (CVPR)*, pp 4700–4708
- Irvin J, Rajpurkar P, Ko M, et al (2019) Chexpert: A large chest radiograph dataset with uncertainty labels and expert comparison. In: *Proceedings of the AAAI conference on artificial intelligence*, pp 590–597

- Jacobs RA, Jordan MI, Nowlan SJ, et al (1991) Adaptive mixtures of local experts. *Neural computation* 3(1):79–87
- Jain S, Agrawal A, Saporta A, et al (????) Radgraph: Extracting clinical entities and relations from radiology reports. In: *Thirty-fifth Conference on Neural Information Processing Systems Datasets and Benchmarks Track (Round 1)*
- Jha D, Sharma V, Dasu N, et al (2023) Gastrovision: A multi-class endoscopy image dataset for computer aided gastrointestinal disease detection. In: *Workshop on Machine Learning for Multimodal Healthcare Data*, Springer, pp 125–140
- Jin H, Che H, Lin Y, et al (2024) Promptmrg: Diagnosis-driven prompts for medical report generation. In: *Proceedings of the AAAI Conference on Artificial Intelligence*, pp 2607–2615
- Johnson AE, Pollard TJ, Berkowitz SJ, et al (2019) Mimic-cxr, a de-identified publicly available database of chest radiographs with free-text reports. *Scientific data* 6(1):317
- Kawahara J, Daneshvar S, Argenziano G, et al (2018) Seven-point checklist and skin lesion classification using multitask multimodal neural nets. *IEEE journal of biomedical and health informatics* 23(2):538–546
- Kawai M, Ota N, Yamaoka S (2023) Large-scale pretraining on pathological images for fine-tuning of small pathological benchmarks. In: *Workshop on Medical Image Learning with Limited and Noisy Data*, Springer, pp 257–267
- Kirillov A, Mintun E, Ravi N, et al (2023) Segment anything. In: *Proceedings of the IEEE International Conference on Computer Vision (ICCV)*, pp 4015–4026
- Krizhevsky A, Sutskever I, Hinton GE (2012) Imagenet classification with deep convolutional neural networks. *Advances in Neural Information Processing Systems* 25
- Lau JJ, Gayen S, Demner D, et al (2018) Visual question answering in radiology (vqa-rad). *Open Science Framework*
- Lewis P, Perez E, Piktus A, et al (2020) Retrieval-augmented generation for knowledge-intensive nlp tasks. *Advances in Neural Information Processing Systems* 33:9459–9474
- Li C, Wong C, Zhang S, et al (2024) Llava-med: Training a large language-and-vision assistant for biomedicine in one day. *Advances in Neural Information Processing Systems* 36

- Li N, Li T, Hu C, et al (2021) A benchmark of ocular disease intelligent recognition: One shot for multi-disease detection. In: Benchmarking, Measuring, and Optimizing: Third BenchCouncil International Symposium, Bench 2020, Virtual Event, November 15–16, 2020, Revised Selected Papers 3, Springer, pp 177–193
- Lin TY, Maire M, Belongie S, et al (2014) Microsoft coco: Common objects in context. In: Proceedings of European Conference on Computer Vision, Springer, pp 740–755
- Lin W, Zhao Z, Zhang X, et al (2023) Pmc-clip: Contrastive language-image pre-training using biomedical documents. In: Proceedings of the Medical Image Computing and Computer Assisted Intervention (MICCAI), Springer, pp 525–536
- Liu B, Zhan LM, Xu L, et al (2021) Slake: A semantically-labeled knowledge-enhanced dataset for medical visual question answering. In: 2021 IEEE 18th International Symposium on Biomedical Imaging (ISBI), IEEE, pp 1650–1654
- Liu H, Li C, Wu Q, et al (2023) Visual instruction tuning. In: Advances in Neural Information Processing Systems, vol 36. Curran Associates, Inc., pp 34892–34916, URL https://proceedings.neurips.cc/paper_files/paper/2023/file/6dcf277ea32ce3288914faf369fe6de0-Paper-Conference.pdf
- Luo L, Wu M, Li M, et al (2024) Towards non-invasive and personalized management of breast cancer patients from multiparametric mri via a large mixture-of-modality-experts model. arXiv preprint arXiv:240812606
- Montalbo FJ (2022) Wce curated colon disease dataset deep learning. <https://www.kaggle.com/datasets/francison/curated-colon-dataset-for-deep-learning>
- Moor M, Banerjee O, Abad ZSH, et al (2023a) Foundation models for generalist medical artificial intelligence. Nature 616(7956):259–265
- Moor M, Huang Q, Wu S, et al (2023b) Med-flamingo: a multimodal medical few-shot learner. In: Proceedings of the Machine Learning for Health (ML4H), PMLR, pp 353–367
- Nakayama LF, Goncalves M, Zago Ribeiro L, et al (2023) A brazilian multilabel ophthalmological dataset (brset). PhysioNet <https://doi.org/10.13026>
- Nguyen HQ, Lam K, Le LT, et al (2020) Vindr-cxr: An open dataset of chest x-rays with radiologist’s annotations. [2012.15029](https://arxiv.org/abs/2012.15029)
- Nguyen HT, Pham HH, Nguyen NT, et al (2021) Vindr-spinexr: A deep learning framework for spinal lesions detection and classification from radiographs. In: Proceedings of the Medical Image Computing and Computer Assisted Intervention (MICCAI), Springer, pp 291–301

- Nguyen HT, Nguyen HQ, Pham HH, et al (2023) Vindr-mammo: A large-scale benchmark dataset for computer-aided diagnosis in full-field digital mammography. *Scientific Data* 10(1):277
- Pacheco AG, Lima GR, Salomao AS, et al (2020) Pad-ufes-20: A skin lesion dataset composed of patient data and clinical images collected from smartphones. *Data in brief* 32:106221
- Panchal S, Naik A, Kokare M, et al (2023) Retinal fundus multi-disease image dataset (rfmid) 2.0: A dataset of frequently and rarely identified diseases. *Data* 8(2). <https://doi.org/10.3390/data8020029>, URL <https://www.mdpi.com/2306-5729/8/2/29>
- Pham HH, Tran TT, Nguyen HQ (2022) Vindr-pcxr: An open, large-scale pediatric chest x-ray dataset for interpretation of common thoracic diseases. *PhysioNet (version 10 0)* 10
- Pogorelov K, Randel KR, Griwodz C, et al (2017) Kvasir: A multi-class image dataset for computer aided gastrointestinal disease detection. In: *Proceedings of the 8th ACM on Multimedia Systems Conference*, pp 164–169
- Radford A, Kim JW, Hallacy C, et al (2021) Learning transferable visual models from natural language supervision. In: *Proceedings of the International Conference on Machine Learning*, PMLR, pp 8748–8763
- Rajbhandari S, Ruwase O, Rasley J, et al (2021) Zero-infinity: breaking the gpu memory wall for extreme scale deep learning. In: *Proceedings of the International Conference for High Performance Computing, Networking, Storage and Analysis*. Association for Computing Machinery, <https://doi.org/10.1145/3458817.3476205>, URL <https://doi.org/10.1145/3458817.3476205>
- Rotemberg V, Kurtansky N, Betz-Stablein B, et al (2021) A patient-centric dataset of images and metadata for identifying melanomas using clinical context. *Scientific data* 8(1):34
- Royer C, Menze B, Sekuboyina A (2024) Multimedeval: A benchmark and a toolkit for evaluating medical vision-language models. [2402.09262](https://doi.org/10.26434/chemrxiv-2024-09262)
- Saab K, Tu T, Weng WH, et al (2024) Capabilities of gemini models in medicine. *arXiv preprint arXiv:240418416*
- Sawyer-Lee R, Gimenez F, Hoogi A, et al (2016) Curated breast imaging subset of digital database for screening mammography (cbis-ddsm). *The Cancer Imaging Archive*, <https://doi.org/10.7937/K9/TCIA.2016.7O02S9CY>
- Silva J, Histace A, Romain O, et al (2014) Toward embedded detection of polyps in wce images for early diagnosis of colorectal cancer. *International journal of computer assisted radiology and surgery* 9:283–293

- Simonyan K, Zisserman A (2014) Very deep convolutional networks for large-scale image recognition. arXiv preprint arXiv:14091556
- Smedsrud PH, Thambawita V, Hicks SA, et al (2021) Kvasir-Capsule, a video capsule endoscopy dataset. *Scientific Data* 8(1):142. <https://doi.org/10.1038/s41597-021-00920-z>
- Subramanian M, Shanmugavadivel K, Naren OS, et al (2022) Classification of retinal oct images using deep learning. In: 2022 International Conference on Computer Communication and Informatics (ICCCI), pp 1–7, <https://doi.org/10.1109/ICCC154379.2022.9740985>
- Tan M, Le Q (2019) Efficientnet: Rethinking model scaling for convolutional neural networks. In: *Proceedings of the International Conference on Machine Learning*, PMLR, pp 6105–6114
- Touvron H, Martin L, Stone K, et al (2023) Llama 2: Open foundation and fine-tuned chat models. arXiv preprint arXiv:230709288
- Tschandl P, Rosendahl C, Kittler H (2018) The ham10000 dataset, a large collection of multi-source dermatoscopic images of common pigmented skin lesions. *Scientific data* 5(1):1–9
- Tu T, Azizi S, Driess D, et al (2024) Towards generalist biomedical ai. *NEJM AI* 1(3):AIoa2300138
- Tung C, Lin Y, Yin J, et al (2024) Exploring vision language pretraining with knowledge enhancement via large language model. In: *International Workshop on Trustworthy Artificial Intelligence for Healthcare*, Springer, pp 81–91
- Van Veen D, Van Uden C, Attias M, et al (2023) Radadapt: Radiology report summarization via lightweight domain adaptation of large language models. arXiv preprint arXiv:230501146
- Wang D, Wang X, Wang L, et al (2023) A real-world dataset and benchmark for foundation model adaptation in medical image classification. *Scientific Data* 10(1):574
- Wang X, Peng Y, Lu L, et al (2017) Chestx-ray8: Hospital-scale chest x-ray database and benchmarks on weakly-supervised classification and localization of common thorax diseases. In: *Proceedings of the IEEE Conference on Computer Vision and Pattern Recognition (CVPR)*, pp 2097–2106
- Wei J, Wang X, Schuurmans D, et al (2022) Chain-of-thought prompting elicits reasoning in large language models. *Advances in Neural Information Processing Systems* 35:24824–24837

- Wu C, Zhang X, Zhang Y, et al (2023a) Pmc-llama: Further finetuning llama on medical papers. arXiv preprint arXiv:230414454
- Wu C, Zhang X, Zhang Y, et al (2023b) Towards generalist foundation model for radiology. arXiv preprint arXiv:230802463
- Xiong C, Chen H, Zheng H, et al (2024) Mome: Mixture of multimodal experts for cancer survival prediction. arXiv preprint arXiv:240609696
- Xu Y, Wang Y, Zhou F, et al (2024) A multimodal knowledge-enhanced whole-slide pathology foundation model. arXiv preprint arXiv:240715362
- Yang J, Shi R, Wei D, et al (2023) Medmnist v2-a large-scale lightweight benchmark for 2d and 3d biomedical image classification. *Scientific Data* 10(1):41
- Yang L, Xu S, Sellergren A, et al (2024) Advancing multimodal medical capabilities of gemini. arXiv preprint arXiv:240503162
- Yu F, Endo M, Krishnan R, et al (2023) Evaluating progress in automatic chest x-ray radiology report generation. *Patterns* 4(9)
- Zhang K, Zhou R, Adhikarla E, et al (2024) A generalist vision-language foundation model for diverse biomedical tasks. *Nature Medicine* pp 1–13
- Zhang X, Wu C, Zhao Z, et al (2023a) Pmc-vqa: Visual instruction tuning for medical visual question answering. arXiv preprint arXiv:230510415
- Zhang X, Wu C, Zhao Z, et al (2023b) Pmc-vqa: Visual instruction tuning for medical visual question answering. arXiv preprint arXiv:230510415
- Zhou HY, Adithan S, Acosta JN, et al (2024) A generalist learner for multifaceted medical image interpretation. arXiv preprint arXiv:240507988
- Zhu D, Chen J, Shen X, et al (2023) Minigpt-4: Enhancing vision-language understanding with advanced large language models. arXiv preprint arXiv:230410592

Appendix A Extended Data

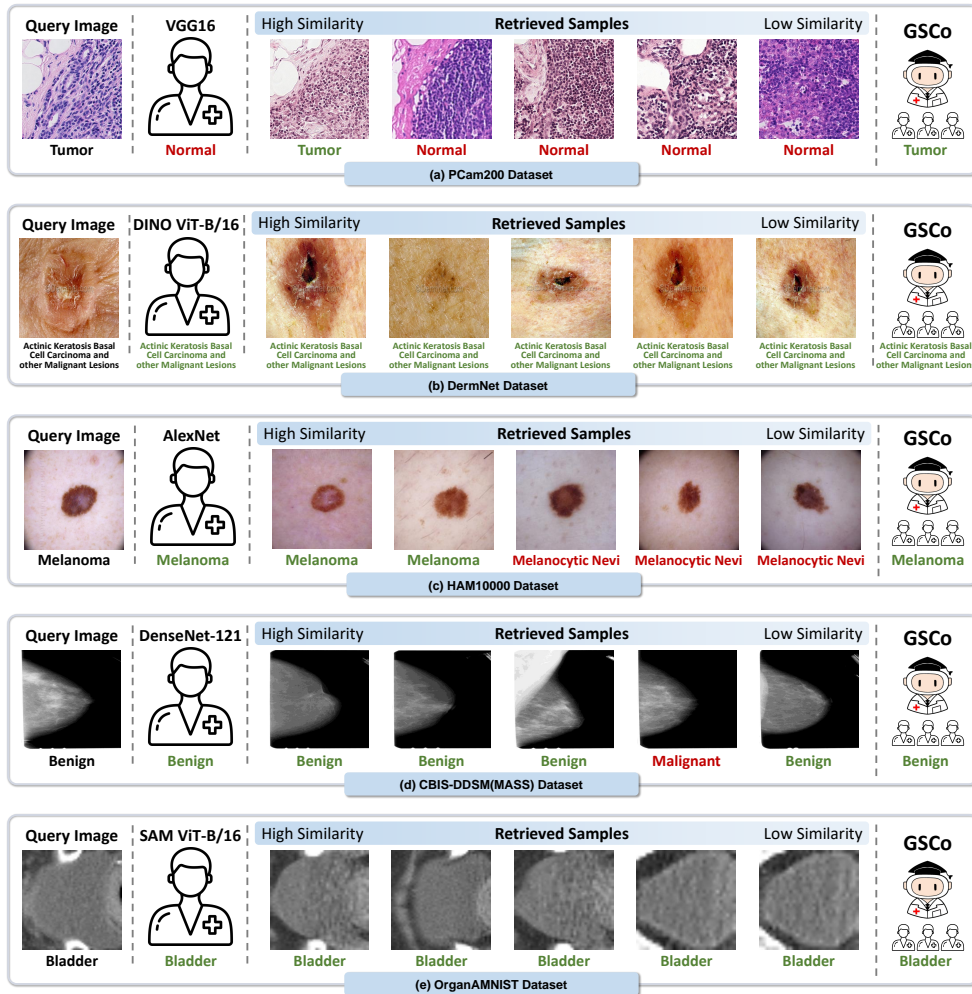


Fig. A1: Examples of Retrieval-Augmented Diagnosis on five downstream medical image diagnosis datasets. From left to right, the contents of each column are: query image and its label, best specialist model and its prediction, Top-5 retrieved similar images and their labels, and prediction of GSCo. **Green** indicates the correct results while **Red** indicates the erroneous results.

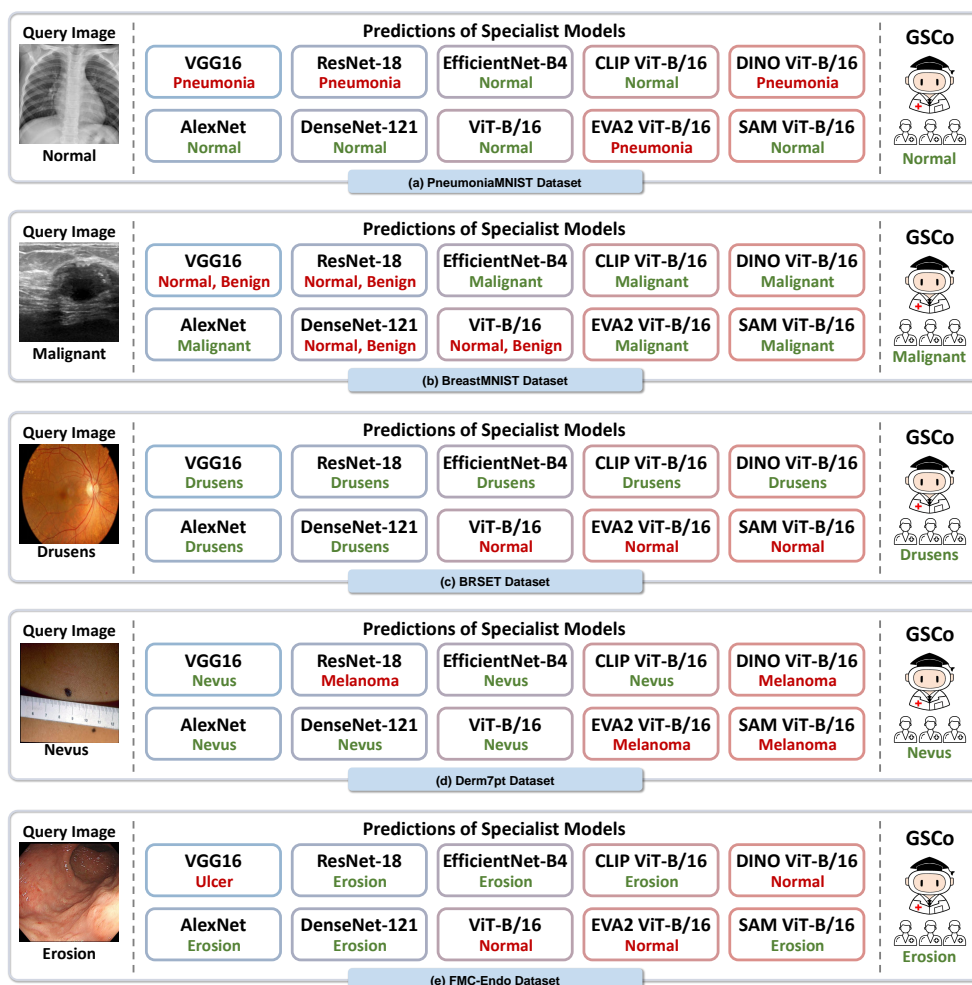


Fig. A2: Examples of Mixture-of-Expert Diagnosis on five downstream medical image diagnosis datasets. Query image and its label, predictions of specialist models, and final diagnosis of GSCo are listed. **Green** indicates the correct results while **Red** indicates the erroneous results.

Table A1: Detailed results on binary classification datasets in medical image diagnosis task. Results are reported in terms of accuracy. **Red** indicates the overall best results, and **Blue** indicates the overall second-best results. **Black** denotes the best results of each model group. Numbers in parentheses indicate a 95% confidence interval (CI).

Method	P Cam200	FMC-Colon	PneumoniaMNIST	BreastMNIST	CBIS-DDSM(MASS)	CBIS-DDSM(CALC)	Average
Generalist Foundation Model							
RadFM	0.4423 (0.4387,0.4459)	0.3851 (0.3779,0.3931)	0.5865 (0.5669,0.6046)	0.3526 (0.3138,0.3919)	0.3889 (0.3651,0.4126)	0.4141 (0.3871,0.4409)	0.4283
LLaVA-Med	0.4986 (0.4951,0.5022)	0.4953 (0.4080,0.4271)	0.5000 (0.4807,0.5192)	0.3782 (0.3408,0.4148)	0.6111 (0.5868,0.6353)	0.6012 (0.5734,0.6275)	0.5141
Med-Flamingo	0.3986 (0.3950,0.4025)	0.3738 (0.3665,0.3810)	0.7131 (0.6957,0.7309)	0.3077 (0.2722,0.3438)	0.6111 (0.5877,0.6349)	0.6043 (0.5790,0.6304)	0.5014
InternVL	0.4986 (0.4949,0.5025)	0.4533 (0.4461,0.4610)	0.4583 (0.4395,0.4763)	0.4615 (0.4221,0.5032)	0.3889 (0.3641,0.4125)	0.3957 (0.3660,0.4211)	0.4427
MedDr	0.9089 (0.9066,0.9110)	0.6262 (0.6184,0.6334)	0.8734 (0.8606,0.8862)	0.7179 (0.6835,0.7541)	0.5132 (0.4871,0.5388)	0.5184 (0.4926,0.5450)	0.6930
Specialist Model							
VGG16	0.9203 (0.9183,0.9223)	0.9621 (0.9593,0.9650)	0.8478 (0.8328,0.8613)	0.8782 (0.8545,0.9016)	0.6614 (0.6378,0.6863)	0.6963 (0.6721,0.7213)	0.8277
AlexNet	0.8340 (0.8314,0.8367)	0.9093 (0.9049,0.9137)	0.8317 (0.8170,0.8453)	0.8782 (0.8497,0.9020)	0.6402 (0.6166,0.6639)	0.6871 (0.6617,0.7117)	0.7968
ResNet-18	0.8816 (0.8794,0.8839)	0.9571 (0.9541,0.9599)	0.8910 (0.8789,0.9026)	0.8590 (0.8322,0.8852)	0.6243 (0.6021,0.6473)	0.5798 (0.5536,0.6062)	0.7988
DenseNet-121	0.9005 (0.8985,0.9026)	0.9575 (0.9544,0.9606)	0.9022 (0.8915,0.9137)	0.8590 (0.8314,0.8849)	0.7011 (0.6795,0.7229)	0.6534 (0.6275,0.6802)	0.8290
EfficientNet	0.8320 (0.8293,0.8348)	0.8094 (0.8949,0.9036)	0.8782 (0.8640,0.8911)	0.7500 (0.7160,0.7835)	0.5556 (0.5309,0.5808)	0.6135 (0.5844,0.6392)	0.7548
ViT	0.9135 (0.9114,0.9156)	0.9240 (0.9202,0.9279)	0.8462 (0.8317,0.8602)	0.8974 (0.8738,0.9195)	0.6693 (0.6457,0.6920)	0.6012 (0.5759,0.6277)	0.8086
CLIP ViT	0.8603 (0.8579,0.8627)	0.9054 (0.9010,0.9096)	0.8478 (0.8337,0.8621)	0.7372 (0.7048,0.7727)	0.6376 (0.6151,0.6613)	0.5920 (0.5628,0.6182)	0.7634
EVA-02 ViT	0.8836 (0.8811,0.8859)	0.9543 (0.9510,0.9573)	0.9038 (0.8931,0.9155)	0.8590 (0.8307,0.8839)	0.6005 (0.5745,0.6250)	0.6166 (0.5908,0.6417)	0.8030
DINO ViT	0.8811 (0.8787,0.8834)	0.9621 (0.9592,0.9649)	0.8141 (0.8000,0.8286)	0.8205 (0.7873,0.8497)	0.6667 (0.6435,0.6897)	0.5982 (0.5710,0.6248)	0.7905
SAM ViT	0.9063 (0.9039,0.9084)	0.9451 (0.9416,0.9485)	0.8814 (0.8689,0.8937)	0.8269 (0.7968,0.8553)	0.6190 (0.5934,0.6434)	0.6564 (0.6307,0.6822)	0.8059
Collaborative Method							
Voting	0.9132 (0.9110,0.9153)	0.9711 (0.9683,0.9733)	0.8702 (0.8558,0.8826)	0.8910 (0.8667,0.9130)	0.6958 (0.6728,0.7168)	0.6564 (0.6316,0.6822)	0.8330
GSCo	0.9321 (0.9302,0.9340)	0.9699 (0.9673,0.9724)	0.9599 (0.9518,0.9670)	0.9295 (0.9091,0.9470)	0.6878 (0.6644,0.7099)	0.6933 (0.6687,0.7177)	0.8621

Table A2: Detailed results on multiclass classification datasets in medical image diagnosis task. Results are reported in terms of macro-F1 score. **Red** indicates the overall best results, and **Blue** indicates the overall second-best results. **Black** denotes the best results of each model group. Numbers in parentheses indicate a 95% confidence interval (CI).

Method	DermiNet	OCTMNIST	PathMNIST	RetOCT	FMC-Endo	OrganAMNIST	HAMI0000	Average	
Generalist Foundation Model									
RadFM	N/A	N/A	N/A	N/A	N/A	N/A	N/A	N/A	
LLaVA-Med	0.0444 (0.0413,0.0476)	1.1305 (0.1219,0.1396)	0.0834 (0.0803,0.0864)	0.1097 (0.0975,0.1244)	0.0586 (0.0552,0.0622)	0.0813 (0.0764,0.0867)	0.0575 (0.0520,0.0632)	0.0871 (0.0806,0.0930)	0.0816
Med-Flamingo	0.0395 (0.0366,0.0428)	1.1000 (0.0953,0.1044)	N/A	0.0755 (0.0703,0.0813)	0.0278 (0.0265,0.0291)	0.0236 (0.0199,0.0276)	0.0484 (0.0476,0.0492)	0.0140 (0.0127,0.0152)	N/A
InternVL	0.1487 (0.1437,0.1538)	0.4542 (0.4427,0.4650)	0.0783 (0.0758,0.0809)	0.1608 (0.1344,0.1882)	0.0892 (0.0856,0.0929)	0.1169 (0.1112,0.1229)	0.0498 (0.0483,0.0514)	0.0478 (0.0413,0.0547)	0.1432
MedDr	0.2995 (0.2926,0.3059)	0.5831 (0.5743,0.5921)	0.2306 (0.2271,0.2342)	0.2331 (0.2031,0.2627)	0.7458 (0.7404,0.7514)	0.3197 (0.2987,0.3426)	0.2066 (0.2041,0.2093)	0.3324 (0.3163,0.3479)	0.3689
Specialist Model									
VGG16	0.4406 (0.4318,0.4489)	0.9337 (0.9263,0.9413)	0.9175 (0.9144,0.9206)	0.1480 (0.1375,0.1634)	0.8180 (0.8153,0.8209)	0.3260 (0.3110,0.3473)	0.9377 (0.9357,0.9396)	0.4815 (0.4636,0.4981)	0.6254
AlexNet	0.4809 (0.4718,0.4896)	0.8594 (0.8484,0.8690)	0.9076 (0.9038,0.9113)	0.1496 (0.1378,0.1626)	0.8020 (0.7982,0.8056)	0.2615 (0.2536,0.2703)	0.9572 (0.9555,0.9589)	0.5688 (0.5477,0.5900)	0.6234
ResNet-18	0.4151 (0.4070,0.4235)	0.8612 (0.8495,0.8716)	0.9186 (0.9147,0.9222)	0.1588 (0.1486,0.1711)	0.8123 (0.8090,0.8154)	0.2801 (0.2728,0.2884)	0.9519 (0.9501,0.9537)	0.4617 (0.4417,0.4819)	0.6075
DenseNet-121	0.5020 (0.4931,0.5104)	0.8201 (0.8084,0.8308)	0.9453 (0.9421,0.9480)	0.1949 (0.1791,0.2134)	0.8126 (0.8095,0.8155)	0.2855 (0.2754,0.2967)	0.9618 (0.9601,0.9634)	0.5137 (0.4943,0.5319)	0.6295
EfficientNet	0.3638 (0.3560,0.3720)	0.8806 (0.8709,0.8906)	0.8939 (0.8899,0.8981)	0.1267 (0.1211,0.1324)	0.7996 (0.7960,0.8032)	0.2649 (0.2565,0.2735)	0.9532 (0.9515,0.9547)	0.3970 (0.3771,0.4180)	0.5850
ViT	0.5535 (0.5447,0.5618)	0.8707 (0.8596,0.8807)	0.9364 (0.9329,0.9397)	0.1990 (0.1747,0.2254)	0.8037 (0.7999,0.8072)	0.2763 (0.2693,0.2830)	0.9642 (0.9627,0.9655)	0.5738 (0.5511,0.5959)	0.6472
CLIP ViT	0.5482 (0.5395,0.5566)	0.8678 (0.8573,0.8776)	0.9325 (0.9291,0.9358)	0.1238 (0.1174,0.1299)	0.6385 (0.6318,0.6454)	0.1521 (0.1490,0.1566)	0.9425 (0.9405,0.9442)	0.3799 (0.3599,0.3990)	0.5732
EVA-02 ViT	0.4875 (0.4793,0.4958)	0.8846 (0.8747,0.8947)	0.9492 (0.9464,0.9522)	0.1416 (0.1294,0.1576)	0.8046 (0.8009,0.8081)	0.1482 (0.1464,0.1500)	0.9616 (0.9602,0.9631)	0.4969 (0.4786,0.5173)	0.6083
DINO ViT	0.5584 (0.5494,0.5666)	0.8343 (0.8227,0.8453)	0.9225 (0.9193,0.9257)	0.3004 (0.2694,0.3273)	0.8040 (0.8005,0.8075)	0.1829 (0.1772,0.1895)	0.9566 (0.9551,0.9582)	0.5576 (0.5351,0.5771)	0.6396
SAM ViT	0.3451 (0.3374,0.3521)	0.9111 (0.9022,0.9195)	0.9392 (0.9358,0.9422)	0.1323 (0.1262,0.1378)	0.7997 (0.7957,0.8034)	0.2570 (0.2478,0.2668)	0.9651 (0.9635,0.9665)	0.4407 (0.4226,0.4600)	0.5988
Collaborative Method									
Voting	0.5883 (0.5784,0.5966)	0.8950 (0.8860,0.9042)	0.9704 (0.9680,0.9728)	0.1431 (0.1377,0.1486)	0.8163 (0.8132,0.8194)	0.2153 (0.2090,0.2216)	0.9792 (0.9781,0.9803)	0.5534 (0.5335,0.5726)	0.6451
GSCo	0.5965 (0.5881,0.6051)	0.9703 (0.9648,0.9751)	0.9626 (0.9600,0.9650)	0.3982 (0.3872,0.4350)	0.9700 (0.9668,0.9730)	0.3511 (0.3273,0.3754)	0.9749 (0.9737,0.9761)	0.5768 (0.5551,0.5967)	0.7251

Table A3: Detailed results on multilabel classification datasets in medical image diagnosis task. Results are reported in terms of macro-F1 score. **Red** indicates the overall best results, and **Blue** indicates the overall second-best results. **Black** denotes the best results of each group (i.e., Generalist Foundation Model, Specialist Model, or Collaborative Method). Numbers in parentheses indicate a 95% confidence interval (CI).

Method	VinDr-PCXR	VinDr-SpineXR	VinDr-Mammo	BRSET	ChestMNIST	FMC-Chest	Average
Generalist Foundation Model							
RadiFM	0.0808 (0.0782,0.0833)	0.1667 (0.1636,0.1701)	0.1389 (0.1373,0.1409)	N/A	0.0491 (0.0476,0.0505)	0.0148 (0.0137,0.0158)	N/A
LLaVA-Med	N/A	N/A	N/A	0.0111 (0.0097,0.0128)	N/A	0.0344 (0.0325,0.0363)	N/A
Med-Flamingo	0.0231 (0.0211,0.0255)	0.0847 (0.0836,0.0859)	N/A	0.0081 (0.0076,0.0087)	N/A	0.0272 (0.0263,0.0281)	N/A
InternVL	0.0695 (0.0667,0.0727)	0.1605 (0.1546,0.1656)	0.0824 (0.0805,0.0843)	0.0214 (0.0183,0.0252)	0.0510 (0.0503,0.0518)	0.0188 (0.0169,0.0211)	0.0673
MedDr	0.0817 (0.0782,0.0856)	0.2682 (0.2613,0.2752)	0.1935 (0.1906,0.1965)	0.0782 (0.0744,0.0827)	0.1339 (0.1319,0.1361)	0.1082 (0.1039,0.1124)	0.1440
Specialist Model							
VGG16	0.0647 (0.0613,0.0680)	0.3548 (0.3433,0.3660)	0.1766 (0.1752,0.1779)	0.3557 (0.3469,0.3645)	0.1292 (0.1268,0.1316)	0.1048 (0.1026,0.1068)	0.1976
AlexNet	0.0775 (0.0729,0.0824)	0.3696 (0.3573,0.3814)	0.1729 (0.1714,0.1741)	0.3051 (0.2922,0.3160)	0.1321 (0.1295,0.1346)	0.1517 (0.1472,0.1559)	0.2015
ResNet-18	0.0644 (0.0613,0.0678)	0.2733 (0.2634,0.2834)	0.1870 (0.1856,0.1884)	0.2462 (0.2391,0.2531)	0.1354 (0.1329,0.1377)	0.0974 (0.0949,0.1000)	0.1673
DenseNet-121	0.0795 (0.0748,0.0843)	0.3293 (0.3194,0.3390)	0.2037 (0.1983,0.2092)	0.3241 (0.3135,0.3331)	0.1578 (0.1551,0.1607)	0.1022 (0.0993,0.1050)	0.1994
EfficientNet	0.0608 (0.0582,0.0638)	0.2920 (0.2811,0.3037)	0.1957 (0.1908,0.2010)	0.2275 (0.2184,0.2371)	0.1097 (0.1078,0.1116)	0.0766 (0.0741,0.0793)	0.1604
ViT	0.0528 (0.0522,0.0534)	0.3035 (0.2957,0.3115)	0.2152 (0.2101,0.2206)	0.3194 (0.3074,0.3311)	0.0893 (0.0875,0.0910)	0.0778 (0.0756,0.0799)	0.1763
CLIP ViT	0.0587 (0.0562,0.0615)	0.2902 (0.2814,0.2987)	0.1767 (0.1752,0.1783)	0.2149 (0.2068,0.2222)	0.0850 (0.0832,0.0868)	0.0705 (0.0675,0.0740)	0.1493
EVA-02 ViT	0.0528 (0.0522,0.0534)	0.2448 (0.2351,0.2534)	0.0993 (0.0982,0.1003)	0.1396 (0.1340,0.1454)	0.0932 (0.0916,0.0946)	0.0455 (0.0439,0.0472)	0.1125
DINO ViT	0.0654 (0.0618,0.0696)	0.3158 (0.3063,0.3258)	0.1764 (0.1750,0.1777)	0.2934 (0.2818,0.3046)	0.1201 (0.1178,0.1223)	0.0847 (0.0821,0.0873)	0.1760
SAM ViT	0.0706 (0.0672,0.0741)	0.1892 (0.1822,0.1969)	0.1767 (0.1746,0.1785)	0.0999 (0.0975,0.1023)	0.0673 (0.0666,0.0681)	0.0607 (0.0586,0.0629)	0.1107
Collaborative Method							
Voting	0.0559 (0.0541,0.0581)	0.2853 (0.2783,0.2924)	0.1886 (0.1873,0.1899)	0.2703 (0.2614,0.2794)	0.0927 (0.0909,0.0946)	0.0813 (0.0791,0.0836)	0.1624
GSCo	0.0859 (0.0814,0.0905)	0.2925 (0.2848,0.3014)	0.2311 (0.2262,0.2364)	0.3342 (0.3226,0.3451)	0.2363 (0.2331,0.2396)	0.1572 (0.1514,0.1634)	0.2229

Table A4: Performance of generalist foundation models on in-domain visual question answering datasets. **Red** indicates the best results, and **Blue** indicates the second best results. ‘*’ means that the model is finetuned on the specific dataset. Numbers in parentheses indicate 95% CI.

Dataset	Metric	RadFM	LLaVA-Med	Med-Flamingo	InternVL	MedDr
VQA-RAD	BLEU-1	48.64 (45.21,51.92)	37.46*	14.23 (12.86,15.52)	55.84 (52.36,59.50)	59.62 (56.24,63.03)
	ClosedAcc	65.34 (61.11,69.86)	22.31*	47.41 (42.86,52.32)	74.50 (70.37,78.57)	78.88 (75.30,82.78)
	OpenRecall	36.83 (32.40,41.63)	63.35* (58.68,68.13)	25.73 (21.75,29.81)	38.77 (34.16,43.44)	37.45 (32.77,42.31)
	Recall	52.70 (49.36,56.30)	38.51* (35.26,41.68)	37.58 (34.28,40.68)	58.65 (55.52,62.11)	60.51 (57.14,63.76)
	OpenAcc	31.50 (26.67,36.30)	59.50* (54.48,64.62)	18.00 (13.74,21.95)	31.50 (26.67,36.59)	30.00 (25.38,34.89)
	F1	50.05 (46.74,53.49)	38.38* (34.93,41.58)	19.98 (18.25,21.74)	57.15 (53.60,60.59)	61.10 (58.05,64.34)
Slake-VQA	BLEU-1	75.22 (73.35,77.25)	66.19* (64.08,68.19)	10.87 (10.09,11.66)	45.70 (43.42,47.86)	76.48 (74.83,78.45)
	ClosedAcc	74.08 (70.87,77.73)	38.87* (35.16,42.86)	46.48 (42.79,50.46)	67.61 (63.84,71.18)	83.38 (80.53,86.28)
	OpenRecall	77.26 (75.04,79.66)	81.55* (79.50,83.58)	27.19 (24.82,29.63)	41.64 (39.01,44.12)	74.18 (71.83,76.47)
	Recall	76.20 (74.32,78.04)	67.27* (65.17,69.30)	32.80 (30.73,34.78)	50.33 (48.02,52.57)	77.26 (75.32,79.17)
	OpenAcc	74.08 (71.70,76.56)	78.19* (75.85,80.69)	22.95 (20.52,25.17)	37.68 (34.92,40.36)	70.53 (67.91,73.20)
	F1	75.98 (74.16,77.86)	66.87* (64.78,69.06)	15.95 (14.81,17.11)	47.07 (44.88,49.14)	77.56 (75.73,79.47)
Path-VQA	BLEU-1	24.89 (24.07,25.71)	44.79* (43.88,45.66)	10.27 (10.00,10.55)	32.67 (31.87,33.53)	61.43 (60.59,62.33)
	ClosedAcc	48.86 (47.68,50.12)	56.00* (54.74,57.21)	57.39 (56.00,58.72)	62.11 (60.88,63.35)	90.21 (89.48,90.94)
	OpenRecall	2.49 (2.15,2.79)	37.91* (36.65,39.10)	6.64 (6.10,7.17)	6.11 (5.59,6.63)	33.47 (32.26,34.61)
	Recall	25.70 (24.84,26.52)	46.07* (45.23,46.91)	32.02 (31.24,32.86)	34.19 (33.38,35.00)	61.92 (61.09,62.78)
	OpenAcc	1.28 (0.99,1.54)	34.87* (33.56,36.13)	4.57 (4.00,5.14)	3.80 (3.31,4.29)	30.50 (29.27,31.68)
	F1	25.24 (24.50,26.03)	45.47* (44.57,46.35)	15.22 (14.78,15.60)	33.20 (32.35,34.05)	62.15 (61.35,63.03)
PMC-VQA	BLEU-1	17.74 (17.59,17.90)	6.65 (6.55,6.74)	9.54 (9.46,9.62)	8.68 (8.6,8.75)	15.22 (15.09,15.34)
	ClosedAcc	79.55 (76.34,82.83)	51.54 (47.64,55.19)	26.89 (23.18,30.42)	40.06 (36.16,43.72)	61.30 (57.27,65.20)
	OpenRecall	20.05 (19.90,20.21)	8.09 (7.98,8.21)	16.30 (16.15,16.44)	23.67 (23.51,23.84)	27.17 (26.99,27.35)
	Recall	20.28 (20.11,20.43)	8.26 (8.15,8.37)	16.34 (16.19,16.48)	23.73 (23.57,23.89)	27.30 (27.12,27.47)
	OpenAcc	11.05 (10.90,11.20)	3.83 (3.74,3.93)	8.08 (7.94,8.21)	11.34 (11.19,11.50)	14.94 (14.75,15.13)
	F1	20.02 (19.86,20.19)	7.98 (7.88,8.09)	12.03 (11.93,12.14)	12.09 (12.00,12.17)	18.90 (18.76,19.02)

Table A5: Performance of generalist foundation models on the VQA-Med dataset. **Red** indicates the best results, and **Blue** indicates the second best results. Numbers in parentheses indicate 95% CI.

Dataset	Metric	RadFM	LLaVA-Med	Med-Flamingo	InternVL	MedDr
VQA-Med	BLEU-1	16.40 (14.87,17.99)	20.91 (14.28,19.27)	7.65 (6.81,8.41)	25.61 (22.89,28.17)	28.87 (26.07,31.96)
	ClosedAcc	57.92 (48.78,66.68)	34.38 (25.63,43.24)	51.39 (41.17,60.54)	57.75 (48.57,67.50)	73.42 (64.86,81.58)
	OpenRecall	27.49 (24.27,30.24)	20.98 (18.19,23.76)	18.75 (16.31,21.23)	22.57 (19.73,25.40)	23.56 (20.77,26.19)
	Recall	31.41 (28.34,34.35)	22.56 (16.06,20.92)	23.02 (20.47,25.62)	27.16 (24.30,29.97)	29.96 (27.03,32.85)
	OpenAcc	25.11 (21.93,28.03)	18.13 (15.44,20.64)	15.69 (13.09,18.18)	20.22 (17.49,23.00)	20.96 (18.08,23.68)
	F1	21.70 (19.70,23.86)	22.35 (16.01,20.78)	11.16 (9.91,12.33)	26.82 (23.98,29.68)	30.51 (27.59,33.35)

Table A6: Performance of generalist foundation models on the OmniMedVQA dataset. Results are reported in terms of accuracy. **Red** indicates the best results, and **Blue** indicates the second best results.

Method	MRI	CT	X-Ray	OCT	Microscopy	Dermoscopy	Fundus	Overall
RadFM	34.37	34.55	38.07	34.46	40.16	30.62	10.76	34.48
LLaVA-Med	25.35	27.79	33.97	37.71	25.34	23.64	30.92	27.05
Med-Flamingo	25.56	28.83	22.11	23.53	30.11	25.31	17.48	26.19
InternVL	63.23	39.59	59.79	46.57	57.22	51.87	67.06	55.61
MedDr	63.58	61.50	71.98	56.52	59.71	57.08	80.67	62.98

Table A7: Ablation Study of the GSCo framework. For binary classification, accuracy is reported. Otherwise, the Macro-F1 score is reported. **Red** indicates the best results, and **Blue** indicates the second best results. Numbers in parentheses indicate the improvement relative to MedDr.

Dataset	MedDr	MedDr+MoED	MedDr+RAD	GSCo
PCam200	0.9089	0.9305 (0.0216↑)	0.9240 (0.0151↑)	0.9321 (0.0232↑)
DermNet	0.2995	0.5788 (0.2793↑)	0.5543 (0.2548↑)	0.5965 (0.2970↑)
HAM10000	0.3324	0.5534 (0.2210↑)	0.5754 (0.2430↑)	0.5768 (0.2444↑)
RetOCT	0.7458	0.9508 (0.2050↑)	0.9671 (0.2213↑)	0.9700 (0.2242↑)
VinDr-SpineXR	0.2682	0.2775 (0.0093↑)	0.2915 (0.0233↑)	0.2925 (0.0243↑)
PneumoniaMNIST	0.8734	0.9535 (0.0801↑)	0.9327 (0.0593↑)	0.9599 (0.0865↑)
BreastMNIST	0.7179	0.8974 (0.1795↑)	0.8974 (0.1795↑)	0.9295 (0.2116↑)
CBIS-DDSM(CALC)	0.5184	0.6503 (0.1319↑)	0.6718 (0.1534↑)	0.6933 (0.1749↑)
PathMNIST	0.2306	0.9301 (0.6995↑)	0.9394 (0.7088↑)	0.9626 (0.7320↑)
Average	0.5439	0.7469 (0.2030↑)	0.7504 (0.2065↑)	0.7681 (0.2242↑)

Table A8: Performance of generalist foundation models on the medical report generation task. **Red** indicates the best results, and **Blue** indicates the second best results. Numbers in parentheses indicate 95% CI.

Dataset	Metric	RadFM	LLaVA-Med	Med-Flamingo	InternVL	MedDr
MIMIC-CXR	F1-RadGraph	18.25 (17.95,18.55)	6.36 (6.22,6.50)	7.13 (6.96,7.29)	6.70 (6.56,6.86)	22.44 (22.13,22.74)
	BLEU-1	22.19 (21.83,22.57)	19.34 (19.09,19.60)	22.43 (22.24,22.64)	25.58 (25.30,25.87)	27.28 (26.83,27.73)
	BLEU-4	5.55 (5.39,5.74)	0.96 (0.92,1.01)	1.91 (1.85,1.98)	1.69 (1.63,1.75)	7.59 (7.39,7.78)
	ROUGE-1	28.88 (28.62,29.09)	21.44 (21.30,21.57)	21.69 (21.54,21.85)	22.87 (22.70,23.04)	32.58 (32.31,32.84)
	ROUGE-L	20.52 (20.31,20.75)	13.90 (13.82,13.98)	14.60 (14.51,14.68)	15.61 (15.51,15.71)	22.59 (22.38,22.79)
	CheXbert Vec	31.18 (30.63,31.73)	15.56 (15.19,15.90)	18.69 (18.30,19.06)	15.90 (15.56,16.26)	34.18 (33.69,34.65)
	METEOR	20.42 (20.19,20.64)	13.25 (13.16,13.34)	14.02 (13.93,14.10)	17.54 (17.44,17.65)	23.77 (23.54,24.05)
	IU-Xray	F1-RadGraph	29.17 (28.62,29.69)	4.72 (4.45,4.97)	11.91 (11.45,12.36)	11.21 (10.81,11.60)
BLEU-1		40.78 (40.32,41.30)	14.85 (14.56,15.14)	16.28 (15.94,16.60)	18.27 (17.93,18.63)	37.71 (36.97,38.50)
BLEU-4		10.28 (9.95,10.61)	0.68 (0.57,0.77)	2.06 (1.93,2.18)	1.73 (1.63,1.83)	12.22 (11.83,12.65)
ROUGE-1		36.79 (36.32,37.23)	12.98 (12.69,13.29)	14.93 (14.60,15.26)	18.22 (17.90,18.56)	39.49 (38.99,39.94)
ROUGE-L		26.07 (25.72,26.42)	9.96 (9.74,10.19)	11.11 (10.88,11.34)	13.43 (13.20,13.66)	28.35 (27.91,28.79)
CheXbert Vec		59.26 (58.26,60.21)	14.01 (13.47,14.57)	24.25 (23.47,24.98)	24.17 (23.48,24.82)	56.47 (55.71,57.34)
METEOR		30.92 (30.44,31.37)	14.48 (14.27,14.72)	17.69 (17.37,18.02)	20.03 (19.74,20.29)	32.34 (31.82,32.92)

Table A9: Performance with retrieval-augmented diagnosis. **Red** indicates the best results, and **Blue** indicates the second best results. Numbers in parentheses indicate 95% CI.

Dataset	Metric	Voting	Med-Flamingo		MedDr	
			w/o RAD	w/ RAD	w/o RAD	w/ RAD
Pneumonia-MNIST	Accuracy	91.03 (89.87,92.13)	71.31 (69.57,73.09)	85.26 (83.89,86.59)	87.34 (86.06,88.62)	92.95 (91.91,93.88)
	Macro-F1	93.15 (92.26,94.02)	76.60 (74.89,78.19)	89.33 (88.16,90.35)	89.16 (88.01,90.28)	94.18 (93.29,94.97)
Breast-MNIST	Accuracy	83.97 (81.01,86.56)	30.77 (27.22,34.38)	58.33 (54.52,62.22)	71.79 (68.35,75.41)	87.82 (85.16,90.30)
	Macro-F1	63.77 (56.91,70.27)	10.00 (6.75,13.99)	55.78 (51.05,60.33)	80.00 (77.20,82.82)	76.54 (71.53,81.08)
OCT-MNIST	Accuracy	67.60 (66.55,68.64)	25.00 (25.00,25.00)	49.40 (48.81,50.00)	67.50 (66.71,68.27)	69.20 (68.10,70.37)
	Macro-F1	62.77 (61.35,64.23)	10.00 (9.53,10.44)	36.34 (35.25,37.40)	58.31 (57.43,59.21)	66.06 (64.66,67.48)
Slake-VQA	BLEU-1	-	0.108 (10.09,11.66)	21.30 (20.31,22.35)	76.48 (74.83,78.45)	77.36 (75.58,79.19)
	ClosedAcc	-	46.48 (42.79,50.46)	63.66 (60.00,67.66)	83.38 (80.53,86.28)	86.20 (83.63,88.94)
	OpenRecall	-	27.19 (24.82,29.63)	36.50 (33.96,39.10)	74.18 (71.83,76.47)	74.31 (72.00,76.60)
	Recall	-	32.80 (30.73,34.78)	45.59 (43.27,47.78)	77.26 (75.32,79.17)	78.29 (76.42,80.08)
	OpenAcc	-	22.95 (20.52,25.17)	31.30 (28.70,33.85)	70.53 (67.91,73.20)	70.25 (67.83,73.11)
	F1	-	15.95 (14.81,17.11)	28.56 (27.18,29.90)	77.56 (75.73,79.47)	78.54 (76.77,80.36)
IU-Xray	F1-RadGraph	31.08 (30.27,31.85)	11.91 (11.45,12.36)	30.35 (29.58,31.06)	33.19 (32.64,33.75)	35.21 (34.54,35.88)
	BLEU-1	40.68 (39.93,41.49)	16.28 (15.94,16.60)	37.65 (36.86,38.48)	37.71 (36.97,38.50)	41.80 (40.94,42.63)
	BLEU-4	12.40 (11.63,13.15)	2.06 (1.93,2.18)	11.34 (10.63,12.01)	12.22 (11.83,12.65)	13.75 (13.11,14.36)
	ROUGE-1	36.74 (36.03,37.36)	14.93 (14.60,15.26)	35.44 (34.74,36.07)	39.49 (38.99,39.94)	40.54 (39.88,41.10)
	ROUGE-L	26.82 (26.14,27.49)	11.11 (10.88,11.34)	25.83 (25.18,26.45)	28.35 (27.91,28.79)	29.54 (28.97,30.09)
	CheXbert Vec	53.57 (52.65,54.44)	24.25 (23.47,24.98)	53.16 (52.22,54.05)	56.47 (55.71,57.34)	57.50 (56.60,58.44)
	METEOR	34.05 (33.28,34.82)	17.69 (17.37,18.02)	33.43 (32.71,34.17)	32.34 (31.82,32.92)	34.09 (33.41,34.78)

Table A10: Detailed information of the in-domain medical image diagnosis datasets. The dataset name, classification type, dataset size, and label set are listed.

Dataset	Type	Size	Label Set
PCam200 Kawai et al (2023)	Binary	17,932	Normal, Tumor.
DermNet Goel (2020)	Multiclass	4,045	Actinic Keratosis Basal Cell Carcinoma and other Malignant Lesions, Atopic Dermatitis, Warts Molluscum and other Viral Infections, Vascular Tumors, Seborrheic Keratoses and other Benign Tumors, Urticaria Hives, Light Diseases and Disorders of Pigmentation, Exanthems and Drug Eruptions, Scabies Lyme Disease and other Infestations and Bites, Psoriasis pictures Lichen Planus and related diseases, Eczema, Poison Ivy and other Contact Dermatitis, Acne and Rosacea, Bullous Disease, Hair Loss Alopecia and other Hair Diseases, Tinea Ringworm Candidiasis and other Fungal Infections, Vasculitis, Lupus and other Connective Tissue diseases, Cellulitis Impetigo and other Bacterial Infections, Melanoma Skin Cancer Nevi and Moles, Systemic Disease, Herpes HPV and other STDs, Nail Fungus and other Nail Disease.
HAM10000 Tschandl et al (2018)	Multiclass	1,511	Actinic keratoses and intraepithelial carcinoma, Basal cell carcinoma, Benign keratosis-like lesions, Dermatofibroma, Melanoma, Melanocytic nevi, Vascular lesions.
RetOCT Subramanian et al (2022)	Multiclass	2,800	Age-related macular degeneration, Choroidal neovascularization, Central serous retinopathy, Diabetic macular edema, Macular hole, Drusen, Diabetic retinopathy, Normal.
ChestMNIST Wang et al (2017)	Multilabel	22,433	Atelectasis, Cardiomegaly, Effusion, Infiltration, Mass, Nodule, Pneumonia, Pneumothorax, Consolidation, Edema, Emphysema, Fibrosis, Pleural, Hernia, No finding
VinDr-SpineXR Nguyen et al (2021)	Multilabel	2,077	Osteophytes, Vertebral collapse, Disc space narrowing, Surgical implant, Other lesions, Foraminal stenosis, Spondylolysthesis, No finding.
VinDr-PCXR Pham et al (2022)	Multilabel	1,397	Pneumonia, Bronchiolitis, Other disease, Bronchitis, Brocho-pneumonia, Tuberculosis, Pleuropneumonia, Situs inversus, Mediastinal tumor, Diaphragmatic hernia, Hyaline membrane disease, Lung tumor, Congenital emphysema, CPAM, No finding.
VinDr-Mammo Nguyen et al (2023)	Multilabel	4,000	Birads negative, Breast heterogeneously density, Breast scattered areas of fibroglandular, Birads suspicious malignant, Mass, Breast extremely density, Birads benign, Birads highly suggestive of malignant, Suspicious Calcification, Breast almost entirely fatty, Suspicious Lymph Node, Focal Asymmetry, Birads probably benign, Asymmetry, Architectural Distortion, Skin Thickening, Global Asymmetry, Nipple Retraction, Skin Retraction, No Finding.

Table A11: Detailed information of the out-of-domain medical image diagnosis datasets. The dataset name, classification type, dataset size, and label set are listed.

Dataset	Type	Size	Label Set
PneumoniaMNIST Yang et al (2023)	Binary	624	Normal, Pneumonia.
BreastMNIST Yang et al (2023)	Binary	156	Normal and Benign, Malignant.
OrganAMNIST Yang et al (2023)	Multiclass	17,778	Bladder, Femur-left, Femur-right, Heart, Kidney-left, Kidney-right, Liver, Lung-left, Lung-right, Pancreas, Spleen.
PathMNIST Yang et al (2023)	Multiclass	7,180	Adipose, Background, Debris, Lymphocytes, Mucus, Colorectal adenocarcinoma epithelium, Smooth muscle, Normal colon mucosa, Cancer-associated stroma.
OCTMNIST Yang et al (2023)	Multiclass	1,000	Choroidal neovascularization, Diabetic macular edema, Drusen, Normal.
CBIS-DDSM(CALC) Sawyer-Lee et al (2016)	Multiclass	326	Benign, Malignant.
CBIS-DDSM(MASS) Sawyer-Lee et al (2016)	Multiclass	378	Benign, Malignant.
FMC-Colon Wang et al (2023)	Binary	4,355	Negative, Positive.
FMC-Endo Wang et al (2023)	Multiclass	2,055	Ulcer, Erosion, Polyp, Tumor, Normal.
FMC-Chest Wang et al (2023)	Multilabel	2,708	Effusion, Nodule, Pneumonia, Cardiomegaly, Hilar enlargement, Fracture old, Fibrosis, Aortic calcification, Tortuous aorta, Thickened pleura, Tb, Pneumothorax, Emphysema, Atelectasis, Calcification, Pulmonary edema, Increased lung markings, Elevated diaphragm, Consolidation, No finding.
Derm7pt Kawahara et al (2018)	Multiclass	395	Nevus, Miscellaneous, Melanoma, Vascular lesion, Lentigo, Melanosis, Dermatofibroma, Basal cell carcinoma, Seborrheic keratosis.
BRSET Nakayama et al (2023)	Multilabel	3,254	Diabetic, Macular edema, Scar, Nevus, Age-related macular degeneration, Vascular occlusion, Hypertensive retinopathy, Drusens, Hemorrhage, Retina detachment, Myopia, Increased cup disc, Disease, Normal.

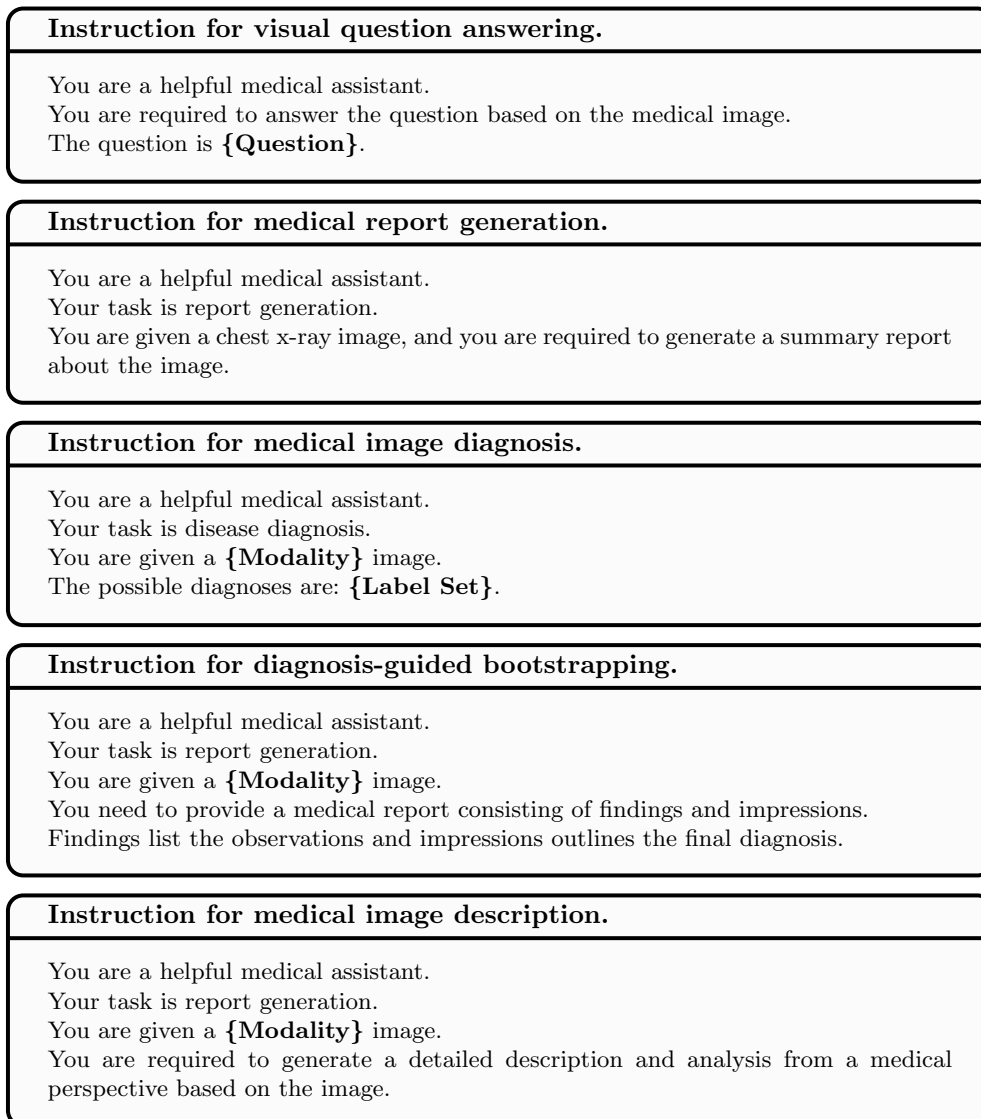


Fig. A3: Prompt templates for different instruction-tuning datasets.

Instructions for Generalist-Specialist Collaboration.

You are a helpful medical assistant.
Your task is disease diagnosis.
You are given a **{Modality}** image.
The possible options are: **{Label Set}**.
The diagnoses of the most similar cases are **{RAD}**.
The reference answers by other models are **{MoED}**.

You are a helpful medical assistant.
Your task is disease diagnosis.
You are required to diagnose the **{Modality}** image.
The reference diagnoses of the most similar cases are **{RAD}**.
The reference answers by other models are **{MoED}**.
The possible options are: **{Label Set}**.

You are a helpful medical assistant.
You are required to classify the **{Modality}** Image.
The reference diagnoses of the most similar cases are **{RAD}**.
The reference answers by other models are **{MoED}**.
The available options are: **{Label Set}**.

You are a helpful medical assistant.
You are required to diagnose the **{Modality}** image.
The reference diagnoses of the most similar cases are **{RAD}**.
The reference answers by other models are **{MoED}**.
The possible options are: **{Label Set}**.

Fig. A4: Instructions for Generalist-Specialist Collaboration. **{Modality}** is the placeholder for the name of different medical modalities. **{Label Set}** denotes the candidate label set of the classification tasks. **{RAD}** and **{MoED}** are the results of retrieval-augmented diagnosis and mixture-of-expert diagnosis.

Table A12: The specifications of the ten selected computer vision models are detailed, encompassing the number of parameters, Giga Multiply-Add Operations per Second (GMACs), and the training time per epoch on a dataset, with PneumoniaMNIST serving as an example. Parameters are quantified in millions (M). “IN1K” refers to ImageNet-1K dataset [Deng et al \(2009\)](#).

Model	Pretrained	Parameters (M)	GMACs	Training Time (sec/epoch)
VGG16 Simonyan and Zisserman (2014)	IN1K	138.4	15.5	15.93
AlexNet Krizhevsky et al (2012)	IN1K	62.3	0.1	3.34
ResNet-18 He et al (2016)	IN1K	11.7	1.8	4.05
DenseNet-121 Huang et al (2017)	IN1K	8.0	2.9	12.91
EfficientNet-B4 Tan and Le (2019)	IN1K	19.3	3.1	15.48
ViT-B/16 Dosovitskiy et al (2021)	IN1K	86.6	16.9	19.35
CLIP ViT-B/16 Radford et al (2021)	CLIP	86.6	16.9	19.28
EVA-02 ViT-B/16 Fang et al (2023)	CLIP	86.3	16.9	23.74
DINO ViT-B/16 Caron et al (2021)	DINO	85.8	16.9	19.14
SAM ViT-B/16 Kirillov et al (2023)	SA-1B	89.7	486.4	24.93

Table A13: Hyperparameters used for training each specialist model. The specific parameters for each model include input dimension, hidden dimension, and dropout rate. The common parameters are batch size, number of epochs, optimizer, learning rate, scheduler, and weight decay.

	VGG16	AlexNet	ResNet-18	DenseNet-121	EfficientNet-B4	ViT-B/16
Input Dim	224×224	224×224	224×224	224×224	224×224	224×224
Hidden Dim	4096	4096	512	1024	1792	768
Dropout	0.0	0.5	0.0	0.0	0.0	0.0

	CLIP ViT-B/16	EVA-02 ViT-B/16	DINO ViT-B/16	SAM ViT-B/16
Input Dim	224×224	224×224	224×224	224×224
Hidden Dim	768	768	768	256
Dropout	0.0	0.0	0.0	0.0

Batch Size	Epochs	Optimizer	Learning Rate	Scheduler	Weight Decay	Cycle Limit
64	100	AdamW	0.0001	Cosine	0.01	1

Table A14: Data availability of training datasets. “Open Access” datasets are freely available to the public. For the “Restricted Access” datasets, please contact the respective dataset providers for access permissions. “Credentialed Access” datasets require specific permissions. “Private” datasets are not publicly accessible.

Dataset Name	Link	Access
Visual Question Answering		
Slake-VQA Liu et al (2021)	https://www.med-vqa.com/slake/	Open Access
VQA-RAD Lau et al (2018)	https://osf.io/89kps/	Open Access
Path-VQA He et al (2020)	https://huggingface.co/datasets/flaviaggiarino/path-vqa	Open Access
PMC-VQA Zhang et al (2023b)	https://huggingface.co/datasets/xmcmic/PMC-VQA	Open Access
PMC-CaseReport Wu et al (2023b)	https://huggingface.co/datasets/chaoyi-wu/PMC-CaseReport	Open Access
Medical Report Generation		
MIMIC-CXR Johnson et al (2019)	https://physionet.org/content/mimic-cxr/2.0.0/	Credentialed Access
IU-Xray Demner-Fushman et al (2016)	https://www.kaggle.com/datasets/raddar/chest-xrays-indiana-university/data	Open Access
Medical Image Classification		
VinDr-SpineXR Nguyen et al (2021)	https://vindr.ai/datasets/spinexr	Credentialed Access
VinDr-PCXR Pham et al (2022)	https://physionet.org/content/vindr-pcxr	Credentialed Access
VinDr-Mammo Nguyen et al (2023)	https://vindr.ai/datasets/mammo	Credentialed Access
VinDr-CXR Nguyen et al (2020)	https://vindr.ai/datasets/cxr	Credentialed Access
CheXpert Irvin et al (2019)	https://stanfordmlgroup.github.io/competitions/chexpert/	Restricted Access
ChestX-ray14 Wang et al (2017)	https://nihcc.app.box.com/v/ChestXray-NIHCC	Credentialed Access
PCam200 Kawai et al (2023)	https://drive.google.com/drive/folders/1Oh7onawKsDW5ScamVO5ByXFgqYJ39sK	Open Access
PAD-UFES-20 Pacheco et al (2020)	https://data.mendeley.com/datasets/zr7vgbcyr2/1	Open Access
DermNet Goel (2020)	https://www.kaggle.com/datasets/shubhamgoel27/dermnet	Open Access
HAM10000 Tschandl et al (2018)	https://www.kaggle.com/datasets/kmader/skin-cancer-mnist-ham10000	Open Access
ISIC2020 Rotemberg et al (2021)	https://challenge2020.isic-archive.com/	Open Access
Kvasir Pogorelov et al (2017)	https://datasets.simula.no/kvasir/	Open Access
Kvasir Capsule Smedsrud et al (2021)	https://datasets.simula.no/kvasir-capsule/	Open Access
WCE Montalbo (2022)	https://www.kaggle.com/datasets/francismon/curated-colon-dataset-for-deep-learning	Open Access
GastroVision Jha et al (2023)	https://github.com/DebeshJha/GastroVision	Open Access
ODIR Li et al (2021)	https://www.kaggle.com/datasets/andrewmvd/ocular-disease-recognition-odir5k	Open Access
Fundus1000 Cen et al (2021)	https://www.kaggle.com/datasets/linchundan/fundusimage1000	Open Access
RFMid2.0 Panchal et al (2023)	https://zenodo.org/records/7505822	Open Access
Retinal OCT-C8 Subramanian et al (2022)	https://www.kaggle.com/datasets/obulisainaren/retinal-oct-c8	Open Access
UltraBreast	-	Private

Table A15: Data availability of benchmark datasets. “Open Access” datasets are freely available to the public. “Credentialed Access” datasets require specific permissions.

Dataset Name	Link	Access
Visual Question Answering		
Slake-VQA Liu et al (2021)	https://www.med-vqa.com/slake/	Open Access
VQA-RAD Lau et al (2018)	https://osf.io/89kps/	Open Access
Path-VQA He et al (2020)	https://huggingface.co/datasets/flaviagiannarino/path-vqa	Open Access
PMC-VQA Zhang et al (2023b)	https://huggingface.co/datasets/xmcmic/PMC-VQA	Open Access
VQA-Med Ben Abacha et al (2019)	https://github.com/abachaa/VQA-Med-2019	Open Access
OmniMedVQA Hu et al (2024)	https://openxlab.org.cn/datasets/GMAI/OmniMedVQA	Credentialed Access
Medical Report Generation		
MIMIC-CXR Johnson et al (2019)	https://physionet.org/content/mimic-cxr/2.0.0/	Credentialed Access
IU-Xray Demner-Fushman et al (2016)	https://www.kaggle.com/datasets/raddar/chester-xrays-indiana-university/data	Open Access
Medical Image Classification		
PCam200 Kawai et al (2023)	https://drive.google.com/drive/folders/1Oh7onawKsDW5ScamVO5ByXFgqYJ39sK	Open Access
Dermnet Goel (2020)	https://www.kaggle.com/datasets/shubhangoe27/dermnet	Open Access
HAM10000 Tschandl et al (2018)	https://www.kaggle.com/datasets/knader/skin-cancer-mnist-ham10000	Open Access
RetOCT Subramanian et al (2022)	https://www.kaggle.com/datasets/obulisainaren/retinal-oct-c8	Open Access
VinDr-SpineXR Nguyen et al (2021)	https://vindr.ai/datasets/spinexr	Credentialed Access
VinDr-PCXR Pham et al (2022)	https://physionet.org/content/vindr-pcxr/1.0.0/	Credentialed Access
VinDr-Mammo Nguyen et al (2023)	https://vindr.ai/datasets/mammo	Credentialed Access
ChestMNIST Yang et al (2023)	https://medmnist.com/	Open Access
PneumoniaMNIST Yang et al (2023)	https://medmnist.com/	Open Access
BreastMNIST Yang et al (2023)	https://medmnist.com/	Open Access
OrganAMNIST Yang et al (2023)	https://medmnist.com/	Open Access
PathMNIST Yang et al (2023)	https://medmnist.com/	Open Access
OCTMNIST Yang et al (2023)	https://medmnist.com/	Open Access
CBIS-DDSM(MASS) Sawyer-Lee et al (2016)	https://www.kaggle.com/datasets/awsaf49/cbis-ddsm-breast-cancer-image-dataset	Open Access
CBIS-DDSM(CALC) Sawyer-Lee et al (2016)	https://www.kaggle.com/datasets/awsaf49/cbis-ddsm-breast-cancer-image-dataset	Open Access
FMC-Colon Wang et al (2023)	https://github.com/openmedlab/MedFM	Credentialed Access
FMC-Endo Wang et al (2023)	https://github.com/openmedlab/MedFM	Credentialed Access
FMC-Chest Wang et al (2023)	https://github.com/openmedlab/MedFM	Credentialed Access
Derm7pt Kawahara et al (2018)	https://derm.cs.sfu.ca/Welcome.html	Credentialed Access
BRSET Nakayama et al (2023)	https://physionet.org/content/brazilian-ophthalmological/1.0.0/	Credentialed Access

Table A16: The public code used in this study.

Name	URL
InternVL Chen et al (2023)	https://github.com/OpenGVLab/InternVL
RadFM Wu et al (2023b)	https://github.com/chaoyi-wu/RadFM
LLaVA-Med Li et al (2024)	https://github.com/microsoft/LLaVA-Med
Med-Flamingo Moor et al (2023b)	https://github.com/snap-stanford/med-flamingo
MedMNIST Yang et al (2023)	https://github.com/MedMNIST/MedMNIST
MedMNIST+ Doerrich et al (2024)	https://github.com/sdoerrich97/rethinking-model-prototyping-MedMNISTPlus
MultiMedEval Royet et al (2024)	https://github.com/corentin-ryr/MultiMedEval